FERMILAB-PUB-12-025-E

Towards a Compensatable Muon Collider Calorimeter with Manageable Backgrounds

Rajendran Raja

Fermilab, P.O. Box 500, Batavia, Illinois 60510

E-mail: raja@fnal.gov

Abstract. Muon Collider detectors pose very challenging problems in detector technology due to extremely large backgrounds present in the detector volume as a result of muon decays. Current designs of a 750 GeV/c per beam Muon Collider envisage 4.28×10^5 muon decays per meter in the beam pipe close to the interaction region. The decay electrons after intense shielding still manage to produce large backgrounds in the detector volume of low energy photons, neutrons and higher energy Bethe Heitler muons. There are 170/184/6.8/177 TeVs energy entering the detector volume per crossing due to EM particles/Muons/Mesons/Baryons respectively. We investigate the capabilities of an iron calorimeter with pixelated readout where each pixel gives a yes/no answer as to whether a charged particle passed through it or not, to solve this problem. Each pixel is individually triggered by a "travelling gate trigger" with a gate of 2 ns where the beginning of the gate is the time of arrival of a light signal from the interaction region to the pixel. We show that such a calorimeter is compensatable and propose two schemes to compensate the digital output in software to improve the resolution of the calorimeter. We show that such a calorimeter is capable of digitizing physics signals from the interaction region and as a result, the backgrounds from the muon decays are much reduced and under control.

1. Introduction

Muon Colliders represent a possible avenue to reach high center of mass energies in lepton-antilepton colliding beams. The resulting collider can be compact and center of mass energies of up to 4 TeV can be contemplated. The Muon Collider scheme, however currently suffers from demonstrating the feasibility of two vital technologies–muon cooling and detectors that can function in the environment of serious background levels introduced by the showering of electrons from decays of muons in the area surrounding the interaction region.

In this paper, we investigate the abilities of a calorimeter with pixelated readout, where each pixel yields a digital yes/no answer as to whether a charged track has passed through it or not. The absorber material is taken to be iron. Each pixel is individually triggerable with a gate g=2 ns. The start of the gate is the time taken for light to travel from the interaction point to the pixel in question. Such a trigger, which we christen, the "traveling gate trigger", minimizes the time the detector is live to the background particles. We show that such a traveling gate trigger can capture the signal event while minimizing the amount of background to be digitized.

The highly pixelated nature of the readout (currently we envisage pixels with linear dimension 200 microns) [1] permits a high degree of pattern recognition in the event which in turn can be used to discriminate against background hits. We show that this pattern recognition ability can be used to separate EM hits and hadronic hits in the calorimeter offline and this in turn can be

Operated by Fermi Research Alliance, LLC under Contract No. De-AC02-07CH11359 with the United States Department of Energy.

MARS Particles in Detector Volume		
Particle Type	**Total Number**	**Total Kinetic Energy (TeV)**
EM	1.785E8	169.9
MUONS	8021.	184.4
MESONS	17589.	6.8
BARYONS	0.409E8	177.4

Table 1. MARS Particles entering the detector volume per crossing in number and Energy as a function of particle type.

used to compensate the calorimeter, yielding much better resolutions. We also introduce a new compensation scheme which counts the number of hadronic vertices in the event and use this to compensate the event yielding better resolutions still.

We demonstrate that the calorimeter with the triggering scheme reduces the backgrounds due muon decays to a manageable level.

2. Backgrounds

2.1. Muon Collider Parameters

We consider a muon collider design [2] of 1.5 TeV center of mass energy with a bunch intensity of 2×10^{12} and one bunch circulating per beam. Such a machine would produce 4.28×10^5 muon decays per meter during the first turn. The muon intensity would drop exponentially due to these decays with a half life of $\approx$ 1000 turns. These high energy electrons, of average energy $\approx$ 250 GeV, (and positrons) from the beam decays would tend to go out of the beam pipe and need to be shielded significantly to avoid severe backgrounds in the detector.

The bunches cross each other every 10 μ seconds. Each bunch has a longitudinal intensity profile of $\pm$ 1 cm at the 1 σ level. This results in an event crossing time jitter of $\approx$ 100 picoseconds at the 3σ level. This is small compared to the triggering gate of 2 ns and we will neglect this time jitter in what follows and assume that the interactions occur at t=0 with respect to the bunch crossing time.

The decays and the electron showers were simulated in [3] using the MARS15 program [4] in a setup as shown in Figure 1. A 10 degree tungsten cone was employed near the beam region to absorb most of the EM showers. However a significant amount of soft particles in the form of photons, electrons neutrons, protons and mesons and harder muons do get through the shielding and reach the detector volume. The particles that reach the interaction region (colored black in Figure 1) are then released by MARS to the user to track through the detector design of choice. Due to the enormous number of decays to be simulated, some of the decay products are weighted. A weight of 20 for a track signifies that only one in 20 such similar particles was tracked through by MARS.

The detector simulator is then presented with a set of particles to be tracked through the detector design that are characterized by a vertex in the interaction region (termed the MARS vertex), the four vector of the track, the time of arrival of the track at the MARS vertex with respect to the crossing time and the weight of the track.

We divide the particles into four categories. EM (electrons, positrons and photons), baryons (neutrons, protons mainly), mesons (charged pions, kaons) and muons. Figure 2 shows the momentum distribution (weighted) of the four categories of background.

Table 1 shows the number of particles and the energy entering the detector volume as a function of particle category. Assuming a calorimeter fractional resolution $\sigma/E) = 50\%/\sqrt{(E)}$, the fluctuation of EM particles alone would be 206 GeV and that of baryons would be 211 GeV per crossing. Given that the total energy of an event cannot exceed 1500 GeV, this background

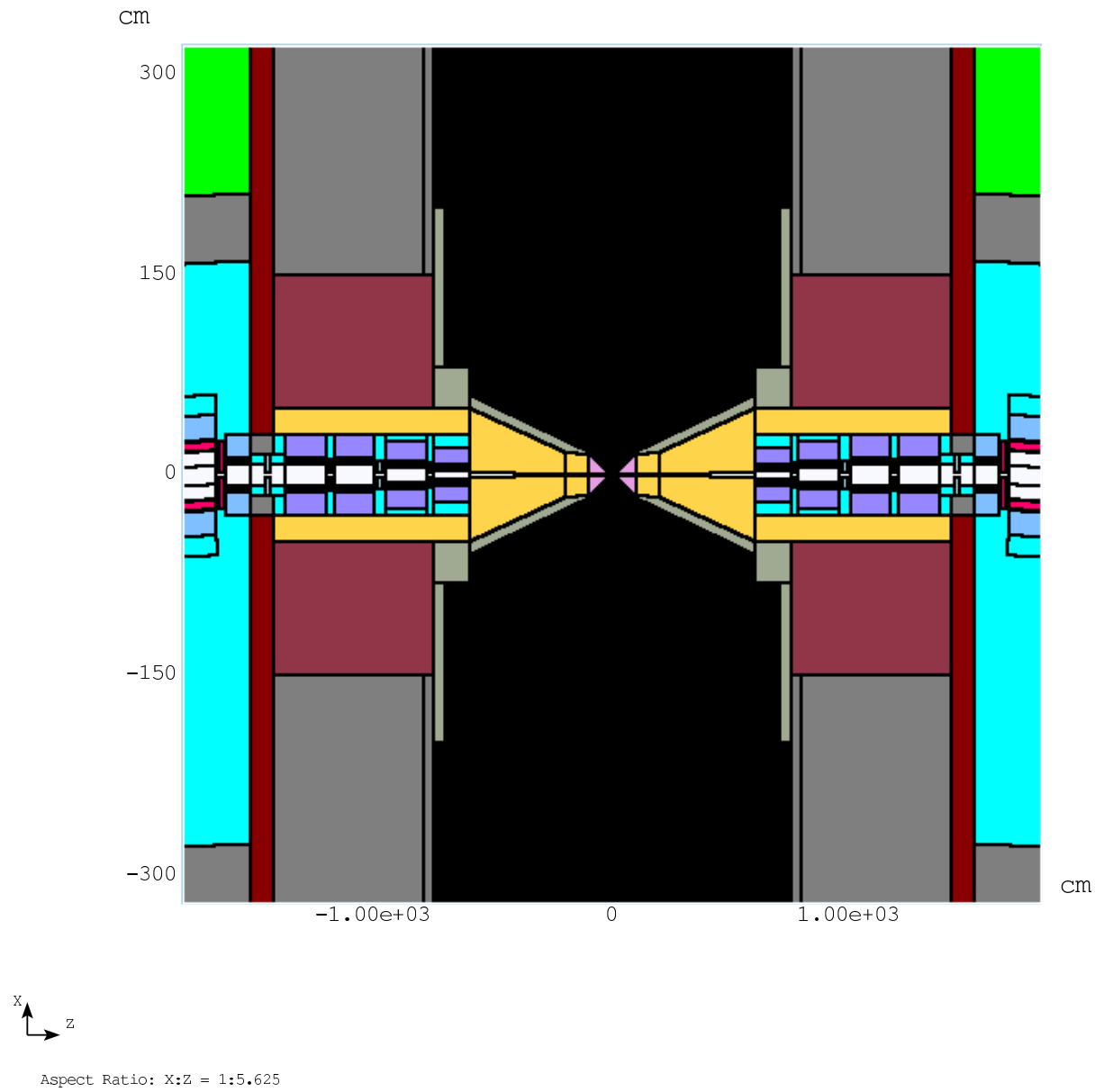

Figure 1. Schematic of the MARS simulation with the 10 degree tungsten cone. The units are in centimeters and the horizontal axis has a different scale from the vertical axis. The muons beams collide in the center of the plot. The yellow part of the picture denotes the tungsten cones that shield a significant portion of the background. When a particle enters the black region, it is passed by MARS to the detector simulation program with its vertex, four vector time of arrival and weight.

presents a formidable challenge to doing physics with a muon collider detector, unless some means are employed to significantly ameliorate the problem. Figure 3 shows the time of arrival of the particles at the MARS vertex with respect to the crossing time. Figure 4 shows the distribution of weights for the four categories. Most of the muon weights are close to unity, where as the other three categories have weights centering around 20. Figure 5 shows the distribution of time taken for light (t_{light}) to travel from the interaction point to the MARS

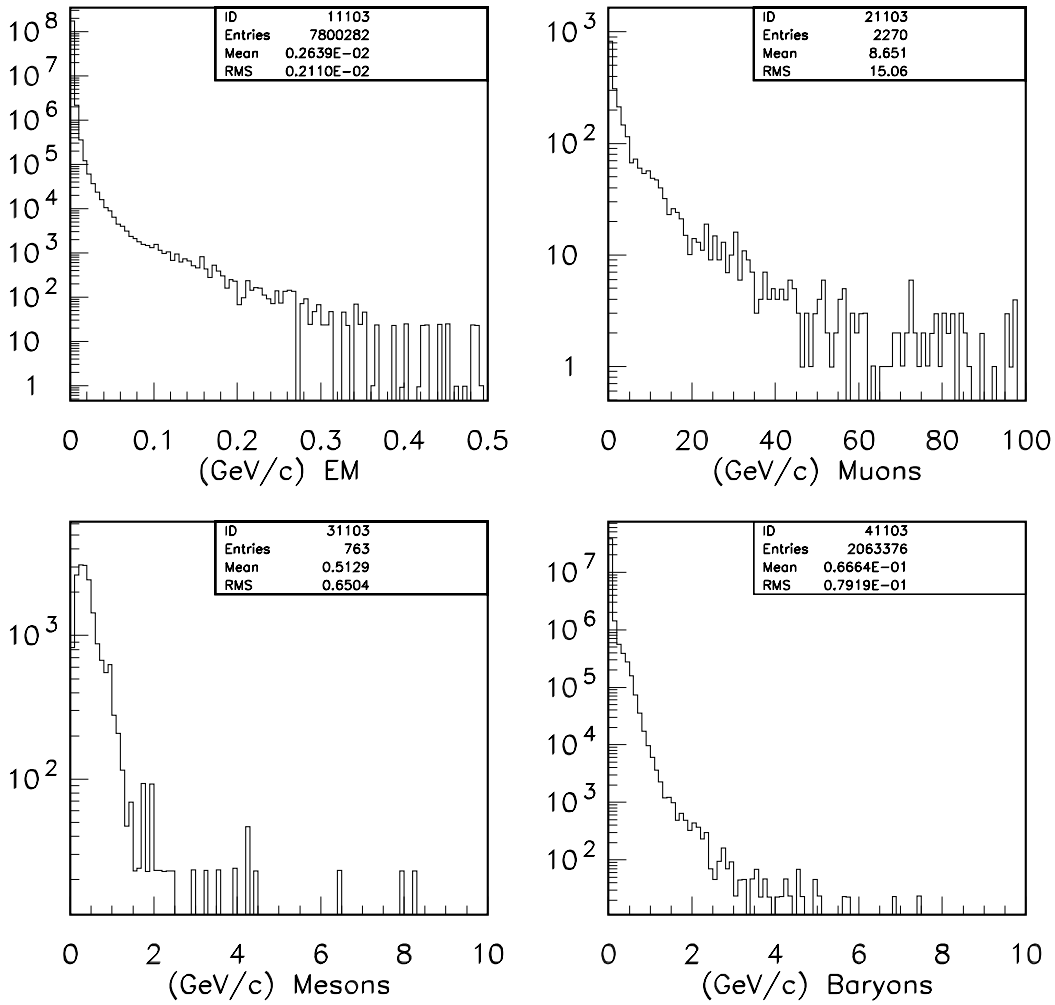

Figure 2. Momentum distribution of the particles comprising of the four categories.

vertex for each particle. Figure 6 shows the quantity δt defined as the difference between the time of arrival of particle at the MARS vertex t_{MARS} and t_{light}.

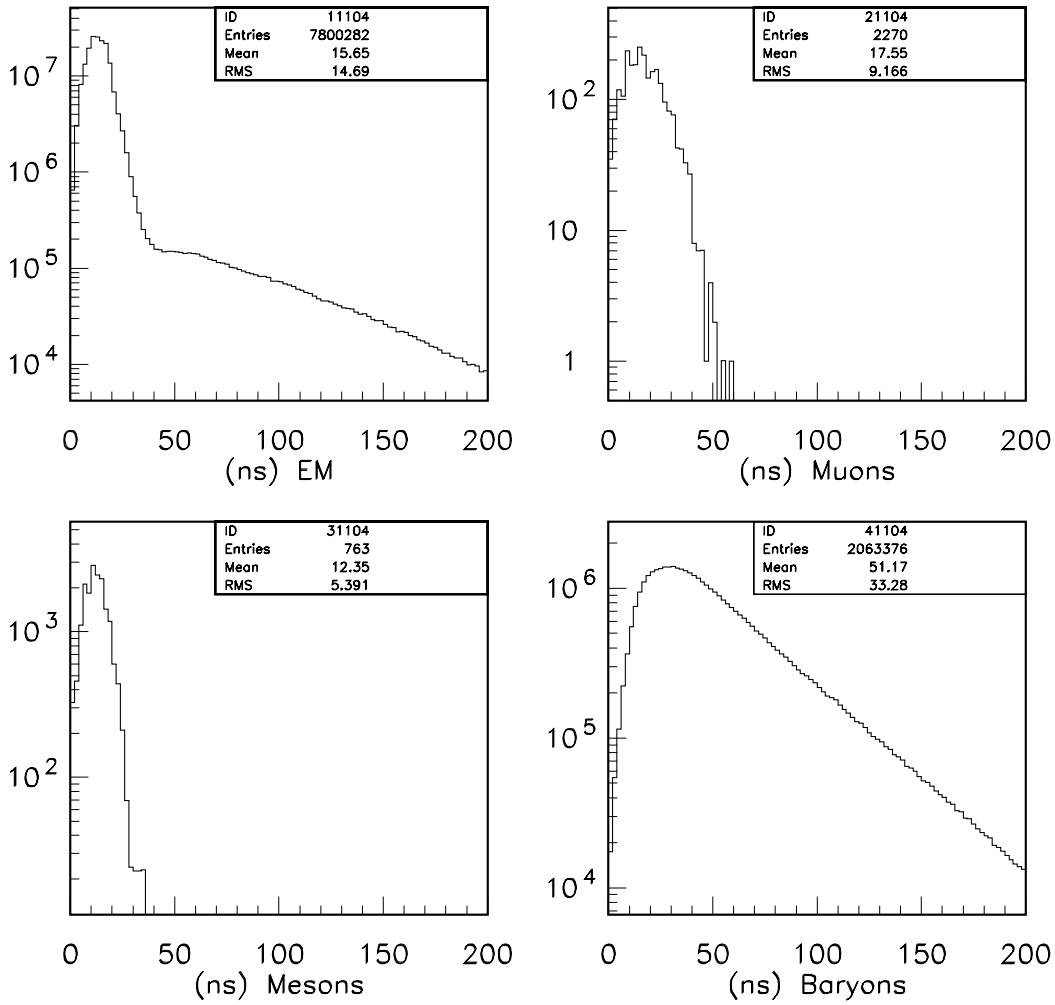

Figure 3. Time of arrival of background particle at the MARS vertex measured with respect to the crossing time for the four categories.

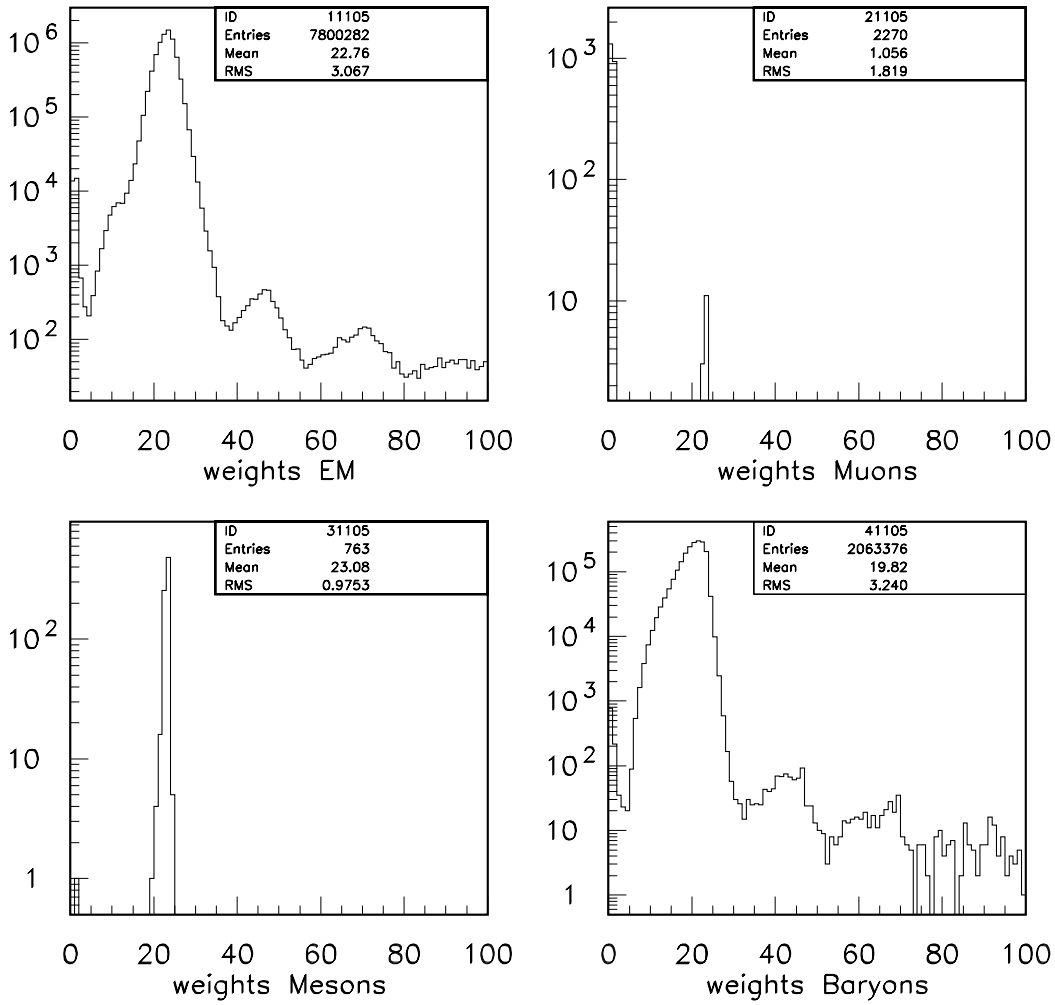

Figure 4. Weight distribution of the particles comprising of the four categories. The average weight for EM particles, mesons and barons is around 20 whereas the muons have weights closer to unity.

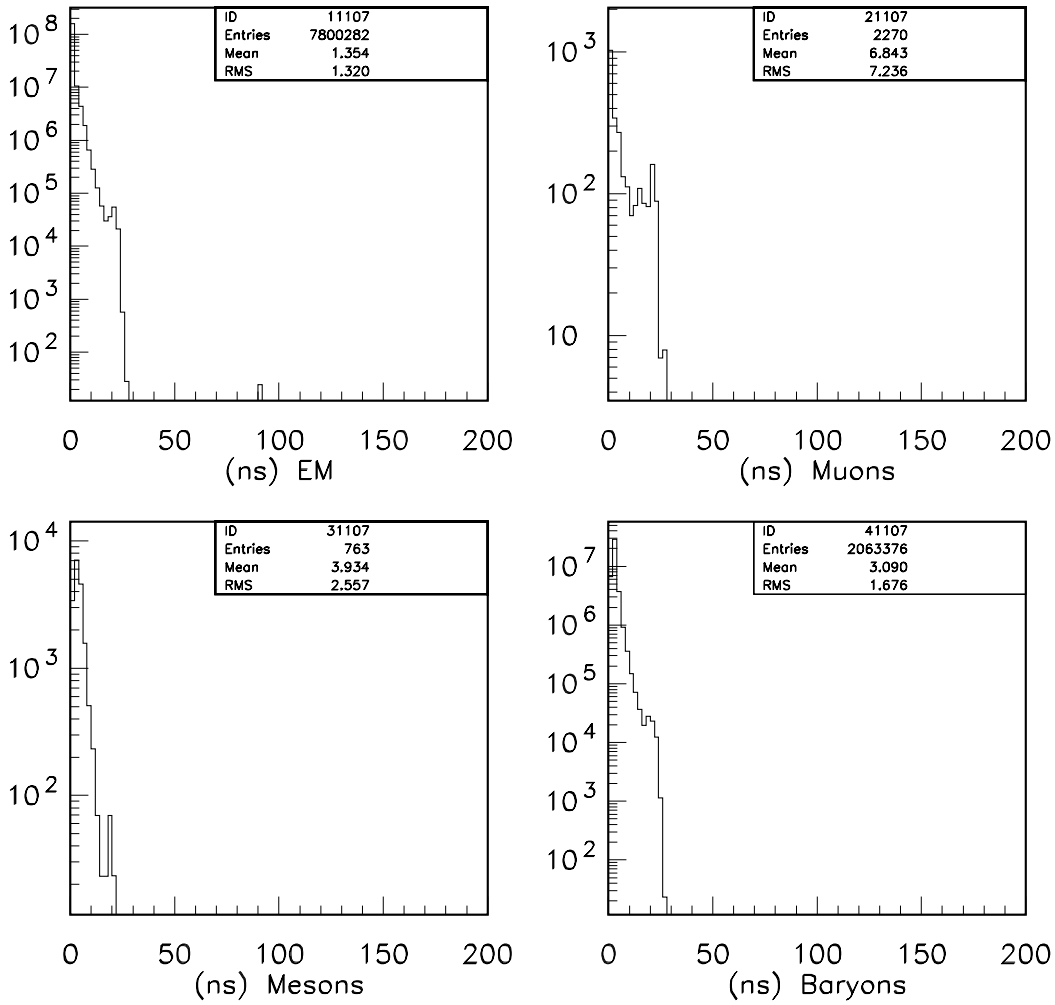

Figure 5. Time taken (ns) for light to travel from interaction point to the MARS vertex for the four categories.

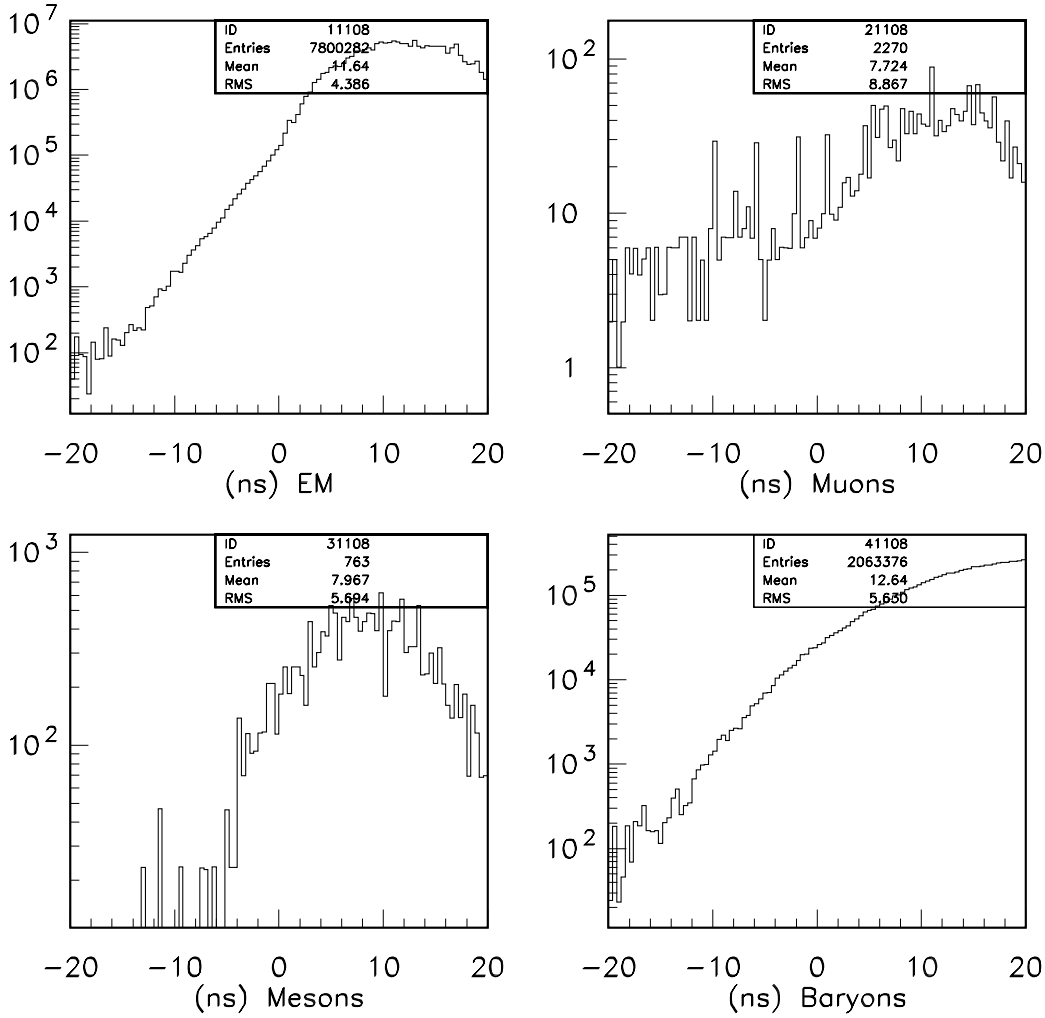

Figure 6. The distribution of $\delta t = t_{MARS} - t_{light}$ for the particles comprising of the four categories.

3. Travelling gate trigger

We define the travelling gate at each pixel as a gate whose start time is the time taken by light to travel from the interaction point to the pixel and the end time is g ns later, where for most of this analysis g is taken to be 2 ns. The time t=0 is defined as that at which the bunches cross.

We now proceed to prove two theorems regarding particle arrival times with respect to the gate. Theorem I states that if at the MARS vertex point the particle in question (MARS vertex is where the MARS program finishes tracking and hands over the track to Geant3 to simulate) is later than the end of the travelling gate at the MARS vertex, then for all subsequent times that particle and all its secondaries will be later than the end of the travelling gate anywhere. This means that all the particles in Figure 6 which lie to the right of $\delta t = 2$ ns can be dropped from further consideration and need not be tracked further. Note that theorem I can be applied inside the MARS program also, and can result in considerable further speedups in MARS program times.

3.1. Proof of Theorem I

We will work in units where the velocity of light is unity. See Figure 7 for a schematic of the geometry. Let t_M denote the time when the particle arrives at the MARS vertex M, t^M_{light} denote the time taken for light to go from the interaction point O to M, i.e. t^M_{light} = OM in our units. Let g denote the gate width. Since the particle arrives at M later than the end of the travelling gate trigger, we get at M,

$$t_M > t^M_{light} + g > OM + g \tag{1}$$

Let t_p denote the arrival time of the particle at P travelling from M.

$$t_p = t_M + t_{MP} \tag{2}$$

For a particle of velocity β, $t_{MP} = MP/\beta$ is the time taken for the particle to travel from M to P. Since $\beta < 1$, this leads to

$$t_p > OM + MP + g \tag{3}$$

But OP is a straight line and thus the shortest distance between O and P. Therefore (as per Euclid),

$$OM + MP > OP \tag{4}$$

leading to $t_p > t^P_{light} + g$ .i.e the particle arrival at P is guaranteed to be later than the end of the travelling gate at P. This applies not only to the particle under consideration but also to all secondary particles caused by any interaction the particle may undergo in the detector. Thus we may safely ignore the particle from further consideration in simulation. Table 2 shows the effect of imposing the Theorem I constraint on the background. Significant reductions are observed in the EM and Baryon categories. The Muon and the Meson categories, being more prompt (i.e. fewer interactions in the shielding) report 23% and 15% survival rates. But there is significant reduction (1.2% and 0.96%) in the categories with the largest amount of energy namely the EM and Baryons.

We now have to track the particles that survive the Theorem I cut in the detector. However, not all of them will be within the travelling gate trigger at all times. Depending on when they appear at the MARS point and which direction they are travelling, they will come into time with the gate and travel some distance before falling out of the gate again. We now calculate the distance an uninteracting particle of velocity β=1 will travel in the calorimeter from the moment it comes into time with the travelling gate to the moment it falls out of the gate.

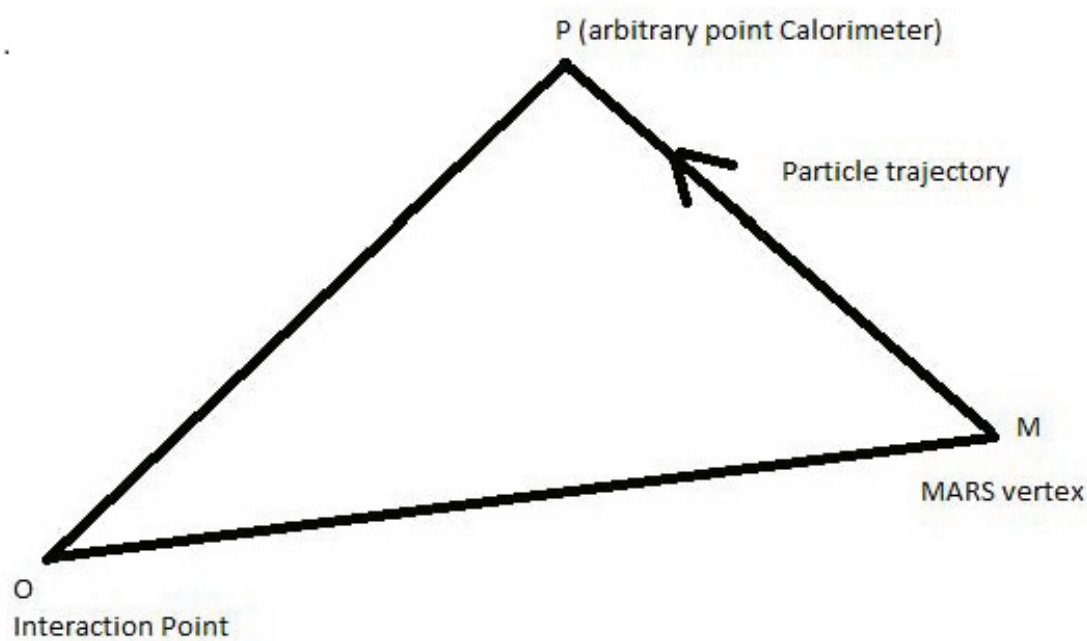

Figure 7. Schematic used to illustrate how Theorem I works. O is the interaction point, M is the MARS vertex point and P is an arbitrary point to which the particle travels from M.

Effect of Theorem I on background			
Particle Type	**Total Number**	$\delta_t < 2$**ns**	**Surviving fraction**
EM	1.79E+08	2.17E+06	1.21E-02
MUONS	8.02E+03	1.83E+03	2.28E-01
MESONS	1.76E+04	2.66E+03	1.51E-01
BARYONS	4.09E+07	3.93E+05	9.62E-03

Table 2. Fraction of MARS Particles entering the detector volume that survive the cut $\delta t < 2ns$ imposed by Theorem I.

3.2. Theorem II

Let M now denote the point at which a particle that passes the Theorem I cut just comes into the travelling gate in Figure 7. Let R denote the distance OM and θ denote the angle 180° - OMP, i.e the obtuse angle in Figure 7. Let d denote the distance MP during which the particle will remain in the gate, going out of the gate at point P. Then for a $\beta = 1$ particle one can show that

$$d = \frac{g(g - 2R)}{2(g - R(1 - cos\theta))} \tag{5}$$

We will see the effect of Theorem II when we examine the Bethe-Heitler muon trajectories in the calorimeter.

4. Proposed Calorimeter Scheme

We investigate the capabilities of an iron calorimeter with 0.4 cm thick iron plates and a pixelated readout with pixels of linear dimension 200 microns. The pixels may be thought of as being made of silicon, though we will indicate possible R&D areas to investigate other options later in the paper. We currently use this size of pixel because we believe it is possible to trigger such a pixel (made of silicon) in 2 ns. Other technologies may permit a larger pixel.

Each pixel is individually triggerable and returns only a yes/no bit indicating whether a charged particle has passed through it or not. No ADC information is demanded i.e. the calorimeter is totally digital. The calorimeter will be employ a sparse readout scheme with only the hit pixels being readout for each event.

4.1. The "Travelling Gate" Triggering Scheme

We assume that the beams cross each other at a predictable time each turn. We then trigger each pixel with a gate of 2 ns which starts at the time taken by light to travel from the interaction region to the pixel. Thus all pixels within a fixed radius from the interaction region will have the same trigger gate. Each pixel can pass on its trigger (delayed electronically by the appropriate amount) to its neighboring pixel for any given module of the readout. Since we do not demand an interaction at the crossing, we may trigger the detector during each crossing, and the detector will be live for each crossing for a period of 2 ns, though not all at the same time. Due the t_{start} being different for different parts of the detector, the live time of the detector will travel at the speed of light starting from the interaction point when the beams cross. After the gate has run through the detector ($\approx$ 30 ns), the calorimeter readout is permitted during the interval till the next beam crossing approximately 10 μ secs later.

4.2. Readout Scheme

We employ a sparse readout scheme, where only the hit pixels are readout.

4.3. Calorimeter and Tracking Geometry

The tracking system in this simulation consists of 20 cylindrical pixel layers placed radially in uniform intervals from 10 cm radius to 79 cm radius. The tracking readout is identical to the calorimetric readout. The number of readout layers can be increased as needed by the demands of pattern recognition. In this study we are merely studying the backgrounds in the tracking system and are not attempting to optimize the tracker.

The calorimeter starts at 80 cm radius and consists of 340 layers, uniform in radius ending at 250 cm. This constitutes 8.11 interaction lengths.

There is no separate EM section in the calorimeter. The first 100 layers of the calorimeter constitute 22 radiation lengths and serve as the EM section.

The traveling gate trigger is applied identically to tracking and calorimetry alike. There is no need for a muon system in this detector since muons are tracks that travel through the calorimeter without interaction.

The length of each layer (tracking and calorimeter) is adjusted so as to fill the detector volume which is delimited by a 10 degree half-angle tungsten cone.

The number of pixels needed in such a scheme is estimated to be addressable with a 41 bit address.

In what follows, we have not smeared the pixel hits with the pixel resolution, nor have we made allowance for two hits being in the same pixel. We will estimate this effect later.

4.4. Magnetic Field
We employ a solenoidal magnetic field such that (for with the positive z axis along the positive muon beam direction),

- $|z|$ <750 cm, B_z = -3.5 Tesla at a transverse radius $r < 330$ cm.
- $B_z = 1.5$ Tesla for $330 < r < 600$ (return field)
- $B_z = 0$ at $r > 600$ cm.
- $B_z = 0$ at $600 < |z| < 750$ cm and at r<10 cm.

This is the same as the field employed in the MARS part of the background simulation.

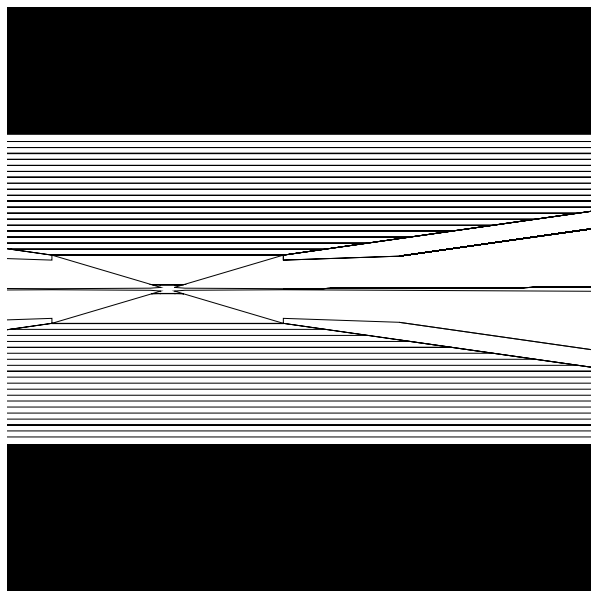

Figure 8. Cut view of the 10 degree cone, tracking layers and calorimeter in the Geant3 simulation.

4.5. Software used
We use a data-driven geometry version of MIPP-Geant3 software [5] to do the simulation. Figure 8 shows the cut view of the detector as implemented in Geant3. The output from Geant3 is digitized in ROOT [6] readable form [7] and output as C_{++} readable files. The geometry from Geant3 is converted to ROOT readable files using standard conversion programs provided by CERN which ensure the usage of a single geometrical system for both simulation and analysis.

The 3D analysis package in ROOT is used extensively in the subsequent analysis as an aid to pattern recognition.

5. Calorimeter Performance
5.1. Calorimeter shower pictures
The calorimeter digitizations from Geant3 on the pixel layers are displayed using ROOT. Figure 9 shows a 100 GeV electron shower in the calorimeter. The first 20 digitizations are the hits

(crosses) in the tracking layer. The calorimeter hits are color coded as follows–hadronic hits are red, electrons cyan, muons green and out of time hits (i.e they fall outside the traveling gate) are in yellow. As can be seen, the electron hits are all in time. The 10 °C forward cone is in magenta. A remarkable amount of detail is available in the digitization about the shower.

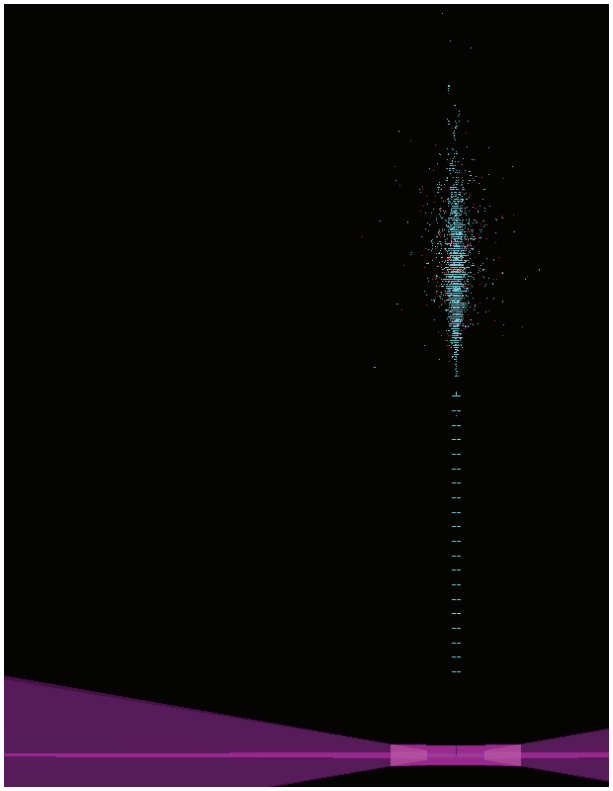

Figure 9. A 100 GeV electron shower in the digital calorimeter.

Figure 10 shows the digitization of a 100 GeV pion shower in the calorimeter. The hadronic tracks can be track followed in software and interact at distinct hadronic vertices. The electromagnetic showers (in cyan) are distinguishable from hadronic tracks by the density of hits in their neighborhood. We will use this fact as well as the ability to count hadronic vertices in devising schemes for software compensation. Figure 11(top) shows the correlation of EM hits in the calorimeter vs hadronic pixel hits in the calorimeter for a sample of 1000 pions of energy 100 GeV each. There is negative correlation between EM hits and hadronic hits. EM and hadronic hits were separated using Monte Carlo truth information. Figure 11(bottom) shows the negative correlation between EM energy and hadronic energy deposited in the calorimeter as measured by the total amount of dE/dx energy deposited in the pixels as well as the iron absorber. We thus show that in hadronic showers of a given energy, the EM energy and hadronic energy are anti-correlated with each other and that the EM hits and hadronic hits show the same behavior. Note in this plot that when the hadronic energy tends to zero (x- axis), the EM energy tends to 100 GeV, showing that the EM energy gives a true measure of the energy scale of the calorimeter. However, when the EM energy tends to zero (y-axis), the hadronic energy approaches $\approx$ 60 GeV, the rest of the hadronic energy disappearing in breaking up nuclei and as undetected neutrons. This is the energy that we have to compensate for.

Figure 12(top) shows the excellent correlation between the number of EM hits in silicon and the amount of EM energy deposited in the calorimeter for 1000 pions of 100 GeV energy.

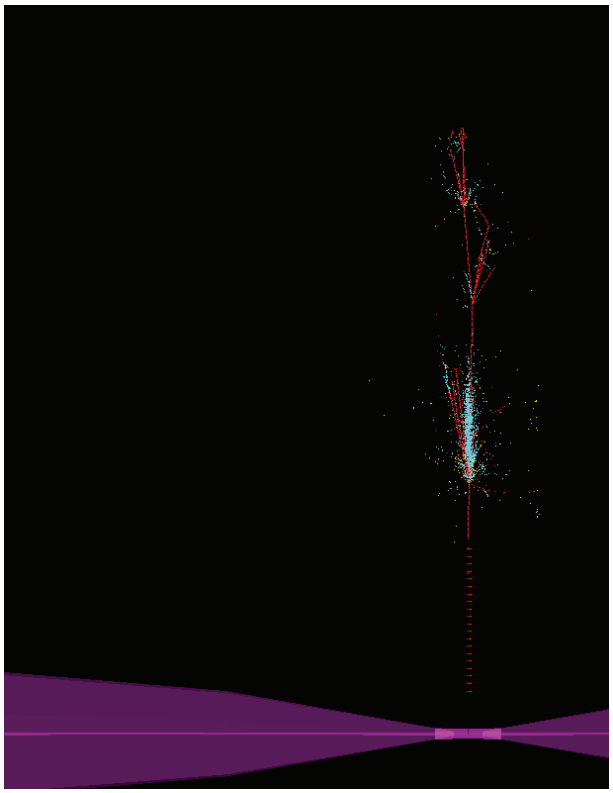

Figure 10. A 100 GeV pion in the digital calorimeter.

The digital hits in silicon track the total energy in EM in the calorimeter. Figure 12(bottom) shows the corresponding plot for hadronic energy, again showing good correlation. Figure 13 shows the correlation between total pixel hits (EM + hadronic) vs total energy deposited in calorimeter for 1000 pions of 100 GeV energy. The total energy deposited does not average to 100 GeV due to the lack of compensation in iron. This is what generates the e/π ratio in iron that is different from unity. However, this plot establishes that the calorimeter hits track the total energy deposited in the calorimeter and the calorimeter can function adequately using digital yes/no information only. In conventional calorimeters, ADC's supply a measure of energy deposited in the readout cell volume. Because of the fine grained nature of the pixel readout, the number of hits summed over any given volume gives the equivalent of the ADC output. The spread in energy in Figure 13 along the y-axis gives rise to the resolution of the calorimeter in measuring hadrons.

Figure 14 shows the average number of hits on the y-axis for a sample of 1000 electrons of energy 10 GeV, 30 GeV and 100 GeV each as a function of the electron energy. We are running Geant3 as a test beam with the interaction point as the origin. Some of the pions decay before inteacting in the calorimeter. These are eletrons with hits < 1000. A slight non-linearity may be observed between the number of hits and the total energy of EM hits due to the number of slow protons in the shower. For lower EM hits, the hadronic energy deposition is slightly larger than for higher EM hits. Slow protons carry dE/dx energy greater than 1 MIP, but they only deposit one hit. There is however sufficient linearity in the EM hits to use this as a calorimeter.

There are two sets of digitizations, within the traveling gate trigger (EM hits time cut) and all times (EM hits). For electrons, there is no loss of signal by using the traveling gate trigger. Figure 15 the average number of hits on the y-axis for a sample of 1000 pions of energy 10 GeV, 30 GeV and 100 GeV each as a function of the true pion energy. There excellent linearity in

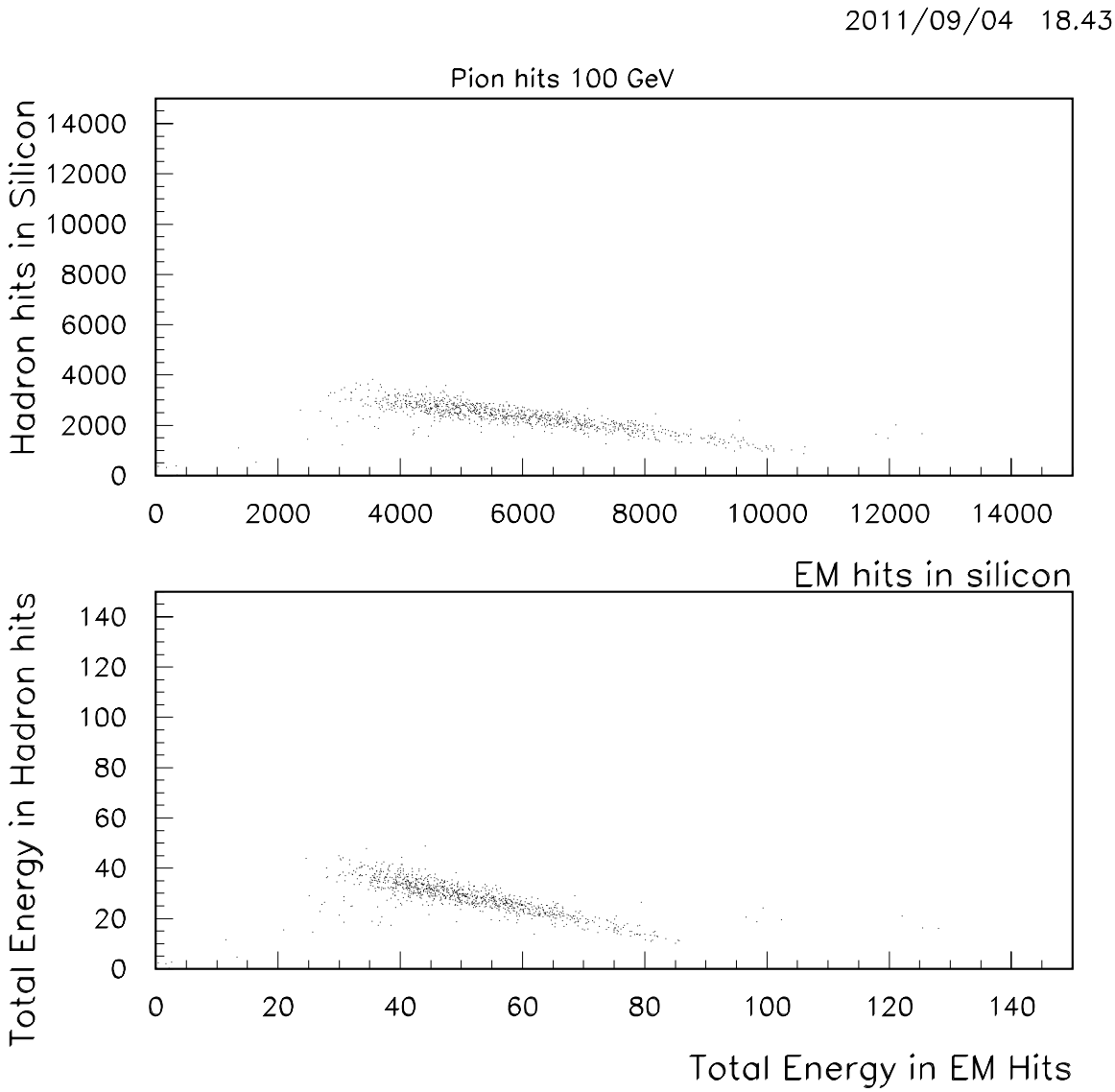

Figure 11. top-Correlation of total number of EM hits in calorimeter vs Hadronic hits in calorimeter for 100 GeV pions. bottom-Correlation of Total EM Energy vs Total Hadronic energy in calorimeter.

the calorimeter for pions. There are two sets of digitizations, within the traveling gate trigger (Silicon hits time cut) and all times (Silicon hits). For pions, there is some loss of signal due to the traveling gate trigger, but the plot is linear in both cases. Note that what is plotted on the abscissa is the true hadron energy and hence questions of compensation do not arise. What this shows is that the calorimeter is linear(enough) for both electrons and pions when true energies are plotted.

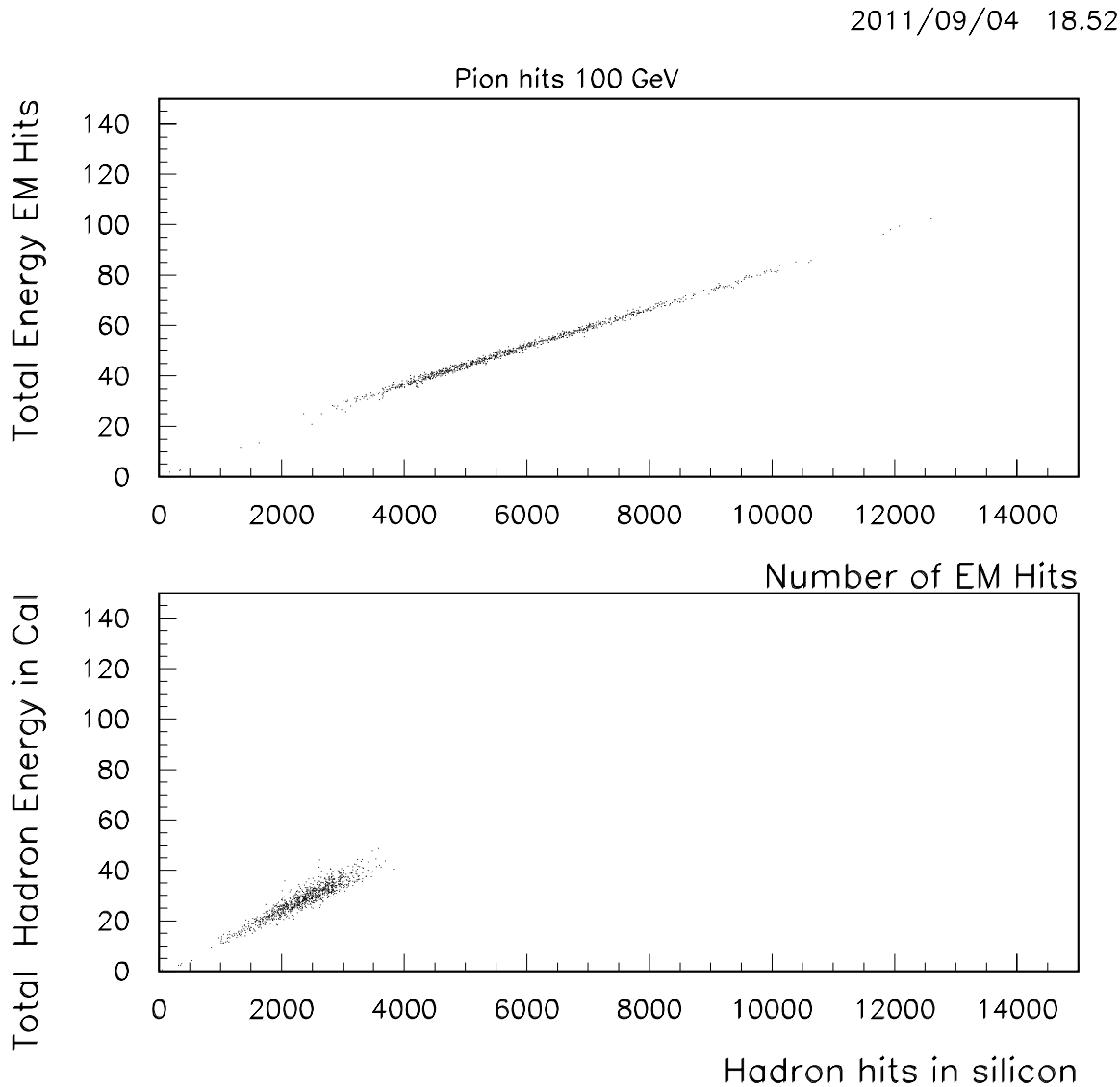

Figure 12. top-Correlation of total number of EM hits in calorimeter vs total EM energy in calorimeter for 100 GeV pions. bottom-Correlation of Total hadronic hits in calorimeter vs total hadronic energy in calorimeter.

5.2. Time of hit vs Radial distance

Figure 16 shows the time of digitization of hits vs radial distance of hit from interaction region for 100 GeV pions. The top plot shows a 2D scatter plot and the bottom plot shows a lego plot of the same. The majority of hits line up along the $\beta = 1$ line. Figure 17 shows the time of digitization of hits for 100 GeV pions with respect to the bunch crossing time. The majority of hits are below t=20 ns, although there is a long tail up to t=500 ns and above. These delayed hits (very small number) are due to a variety of processes that involve nuclear excitation and subsequent decay as a result of the passage of the shower. Figure 18 shows the histogram of the traveling gate trigger variable $\delta t \equiv t_{digitization} - t_{light}$ for hits from an ensemble of 100 GeV pions.

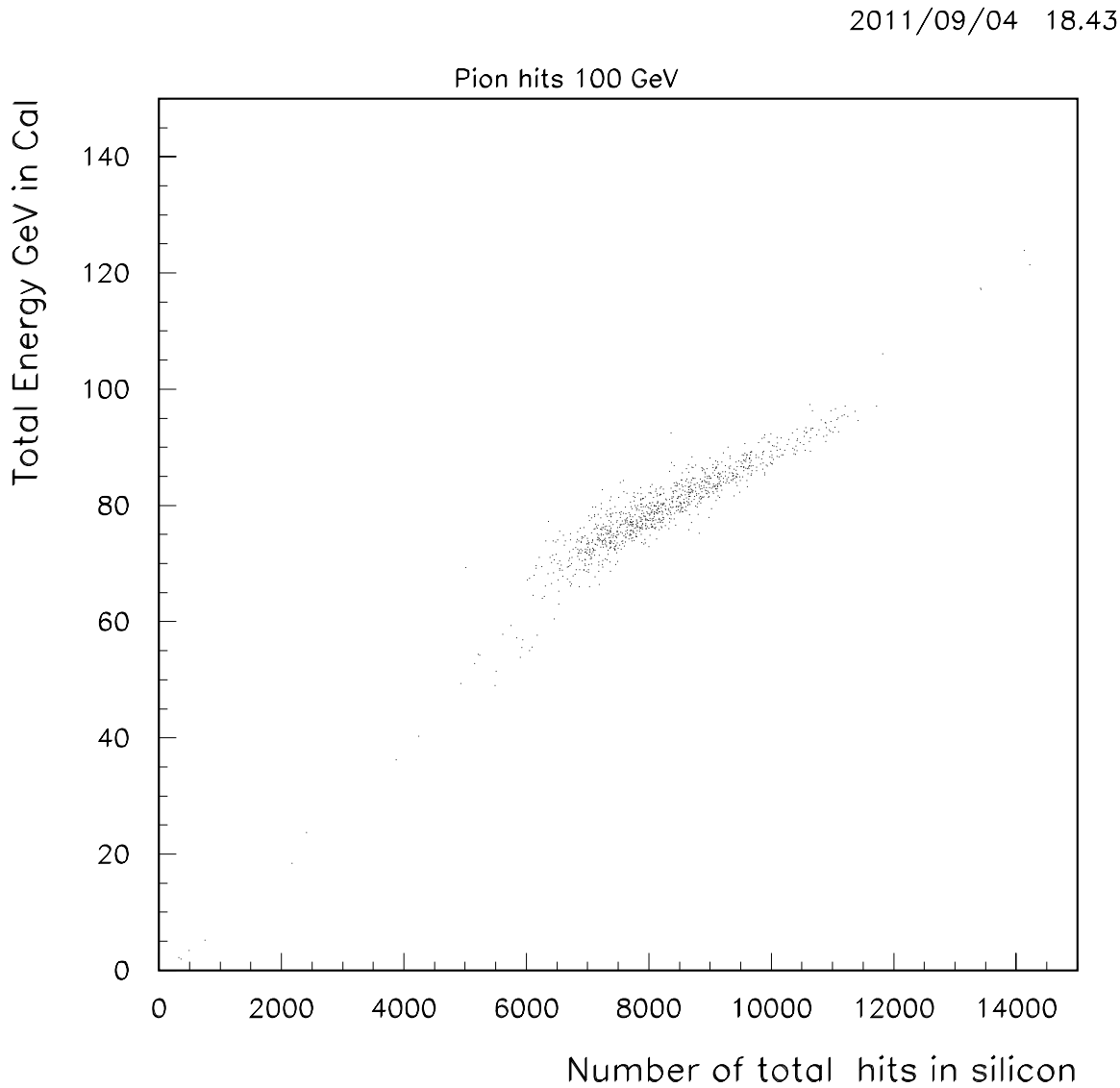

Figure 13. Total number of pixel hits vs total Energy in calorimeter for 100 GeV pions.

The vast majority of hits lie below $\delta t = 2\ ns$, there is a long tail due to nuclear excitations, which as we will show now, contributes little to the energy measurement of the shower. Figure 19 shows the energy fraction of the electron shower digitized as a function of δt for ensemble of 1000 electrons of 1 GeV, 10 GeV, 30 GeV and 100 GeV energies. All the electrons produce shower particles which are very close to $\beta = 1$ and there is no loss of signal as δt is reduced to the gate width of 2ns. Figure 20 shows the energy fraction of a pion shower digitized as a function of δt for an ensemble of 1000 pions of 1 GeV, 10 GeV, 30 GeV and 100 GeV energies. There is some loss of energy digitized as the gate δt is reduced to 2 ns, which depends on the energy of the primary pion. However, this small non-linearity in the hadronic calibration scale can be corrected for offline since the detector is capable of recognizing individual hadronic showers. We thus conclude that a traveling gate trigger with a gate 2 ns results in a calorimeter that can

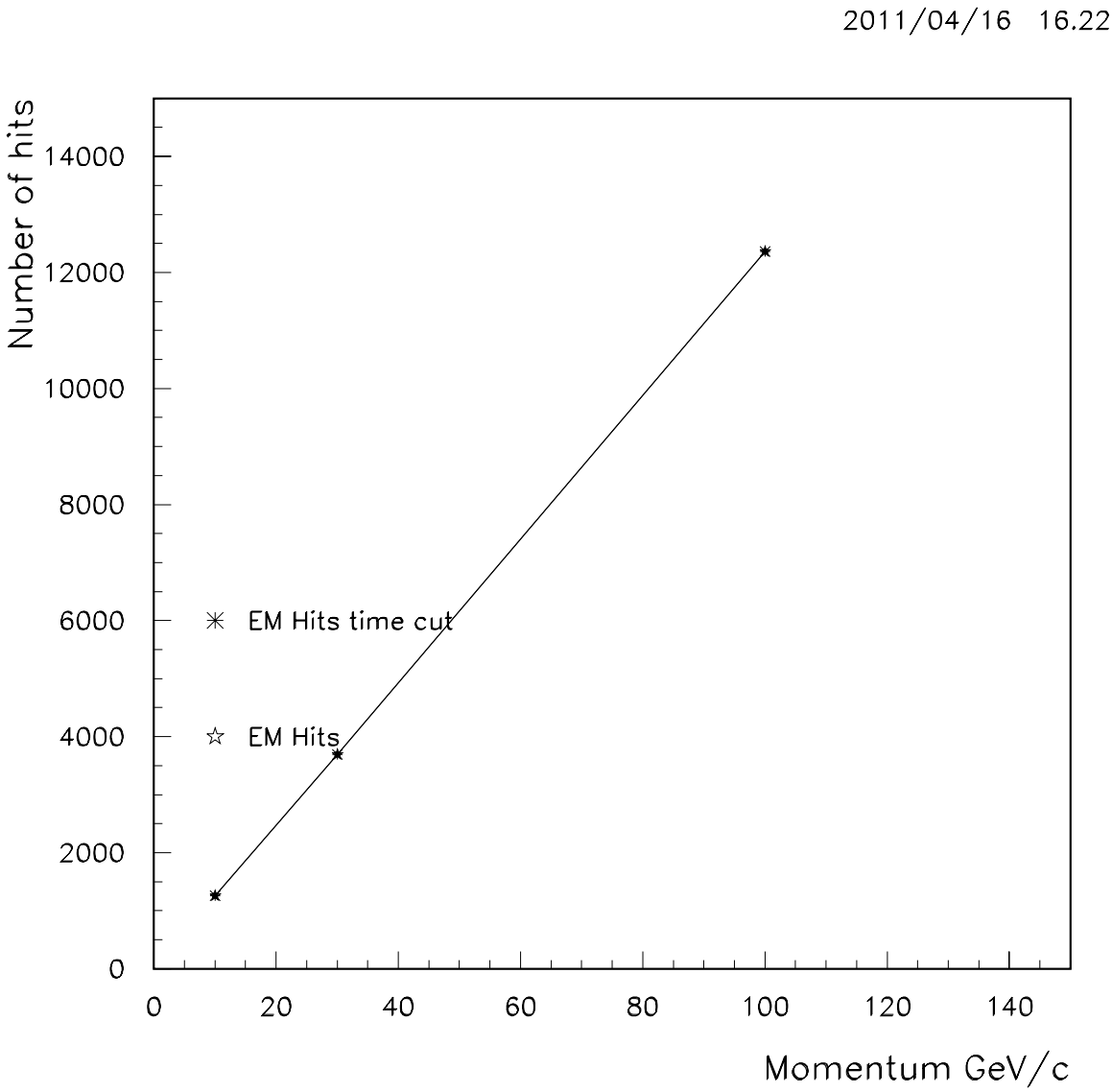

Figure 14. Number of pixel hits in calorimeter vs Momentum for electrons with and without traveling gate trigger.

digitize all events.

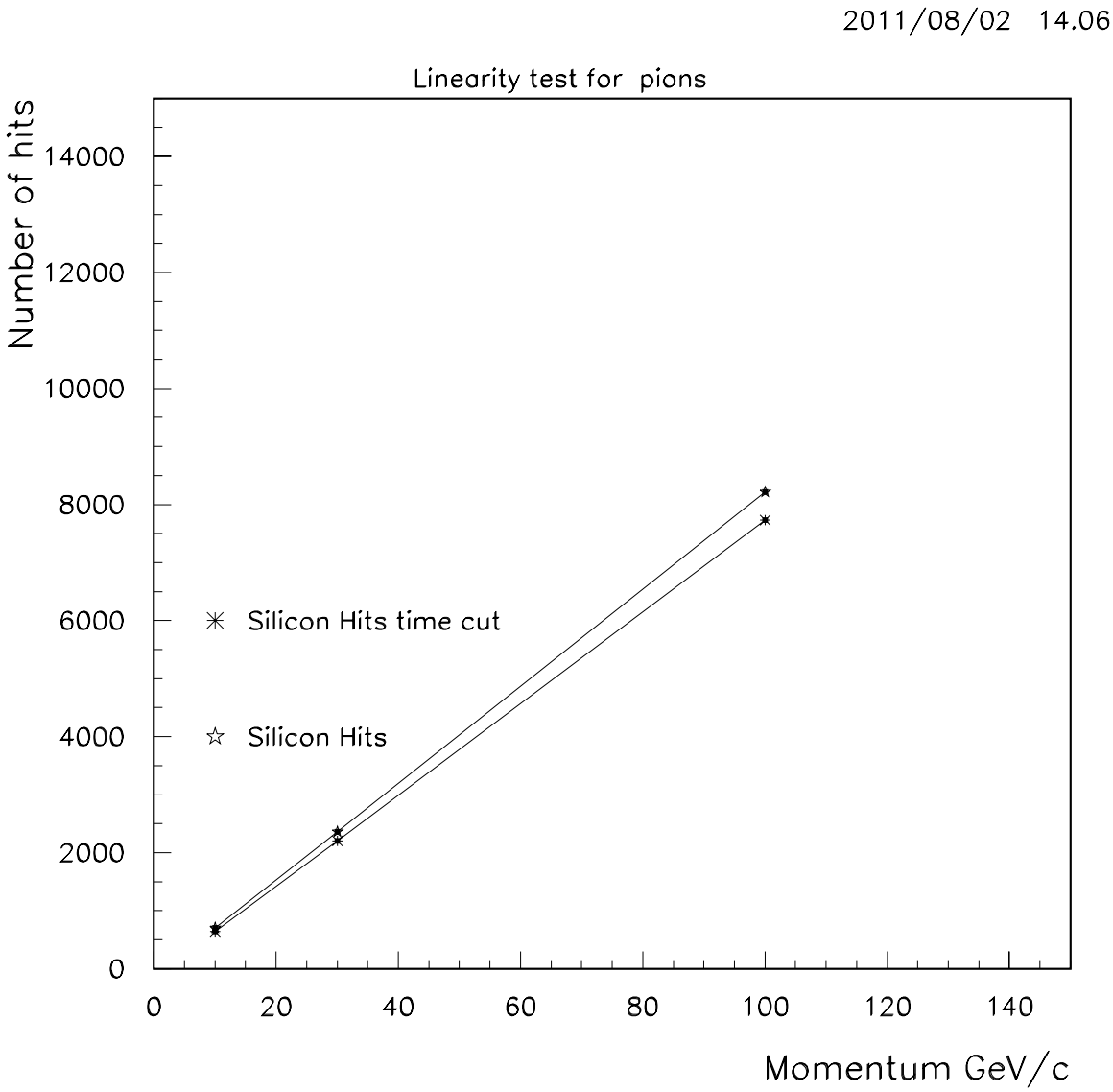

Figure 15. Number of pixel hits in calorimeter vs Momentum for pions with and without traveling gate trigger.

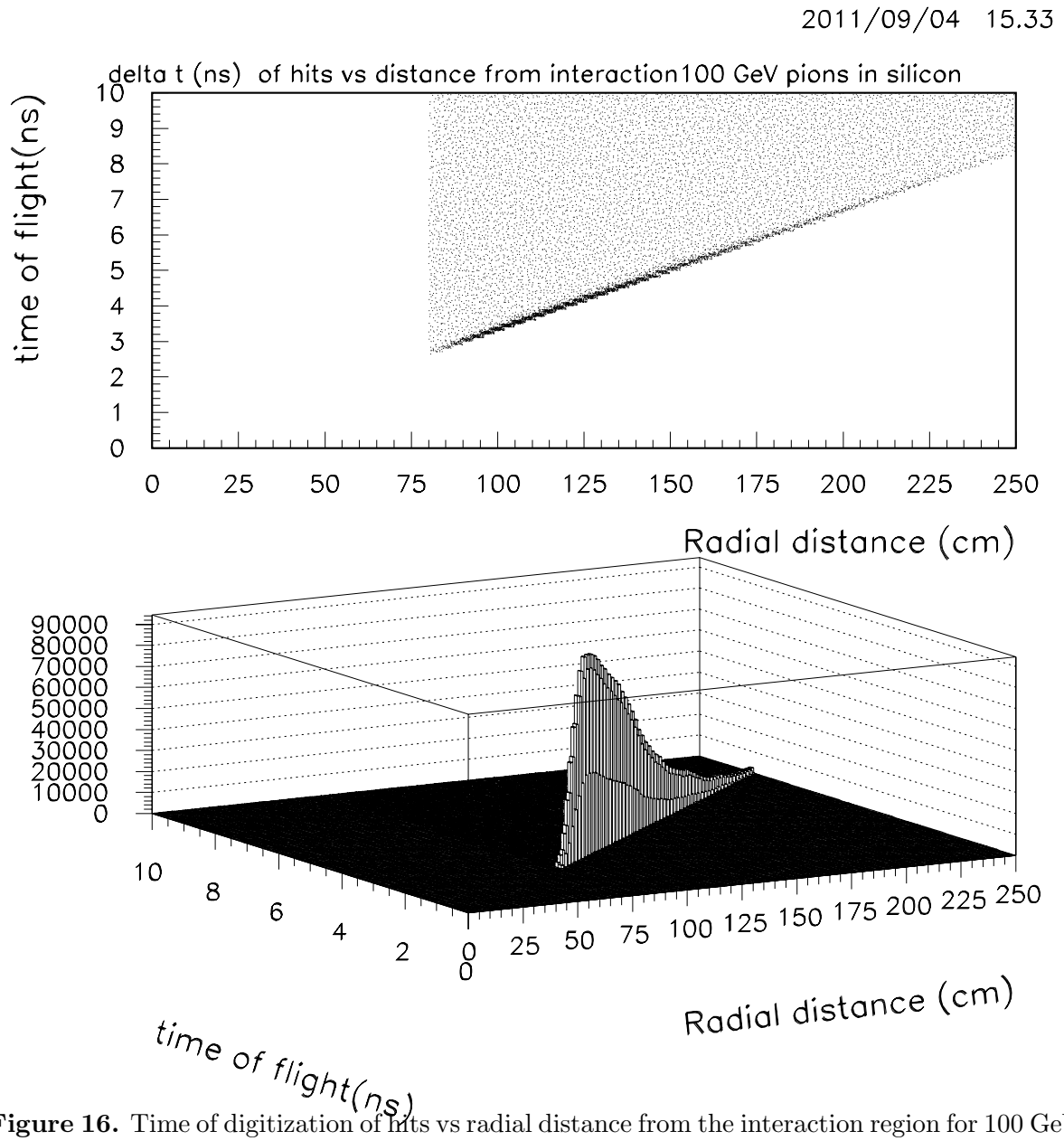

Figure 16. Time of digitization of hits vs radial distance from the interaction region for 100 GeV pions–top 2D scatter plot bottom–Lego plot. (Correct title)

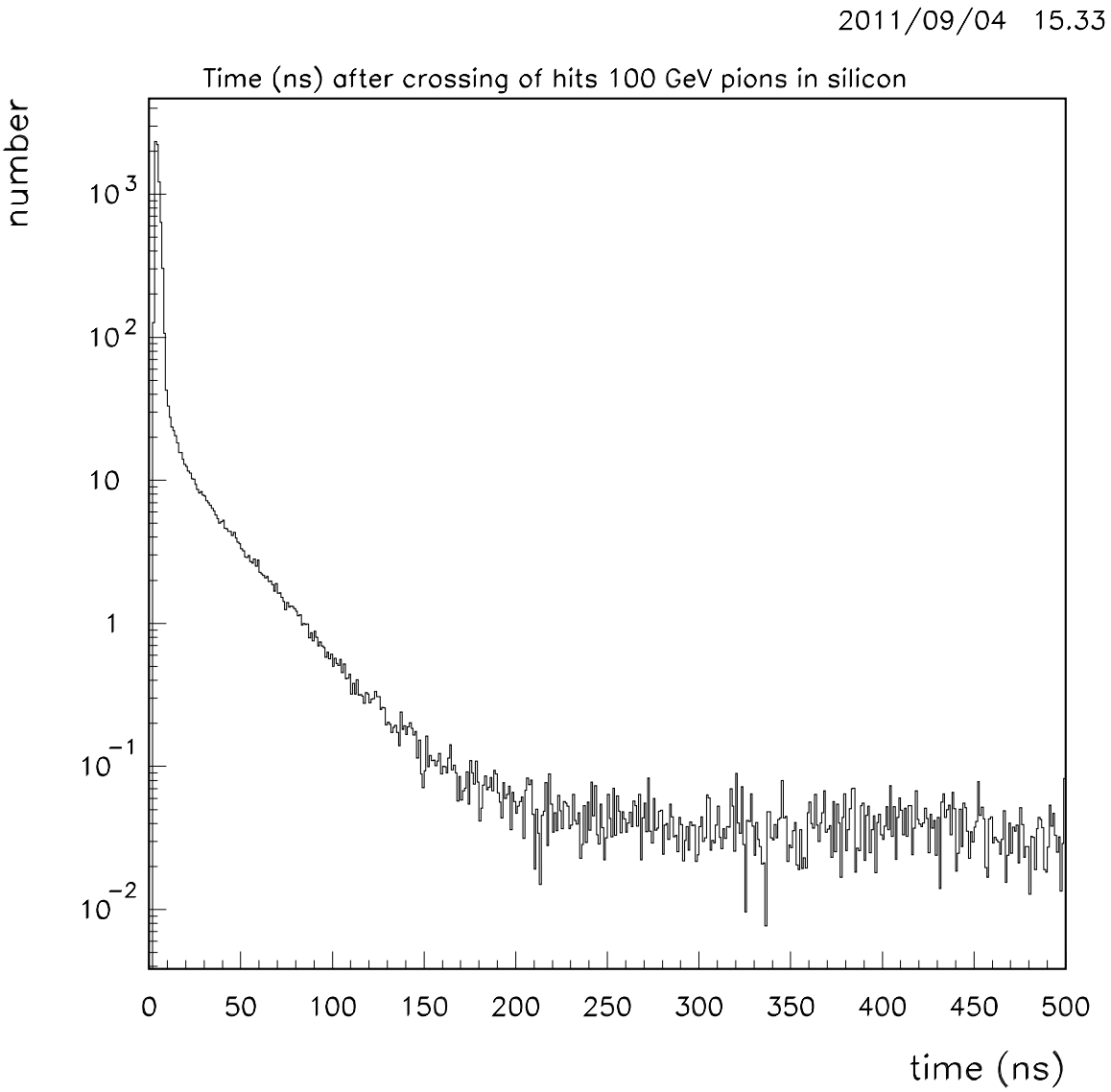

Figure 17. Time of digitization of hits for 100 GeV pions

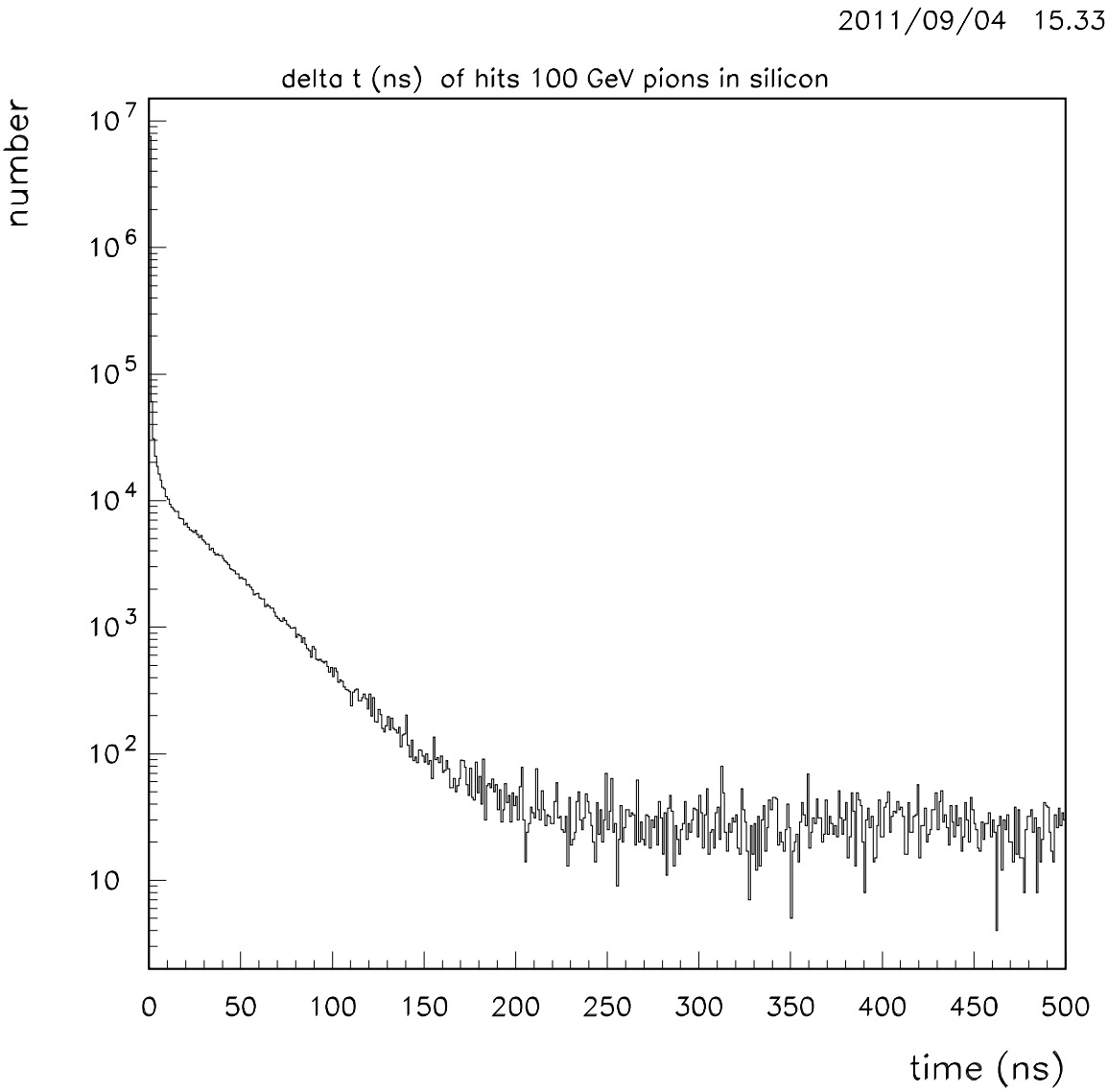

Figure 18. $\delta t = t_{digitization} - t_{light}$ hits for 100 GeV pions

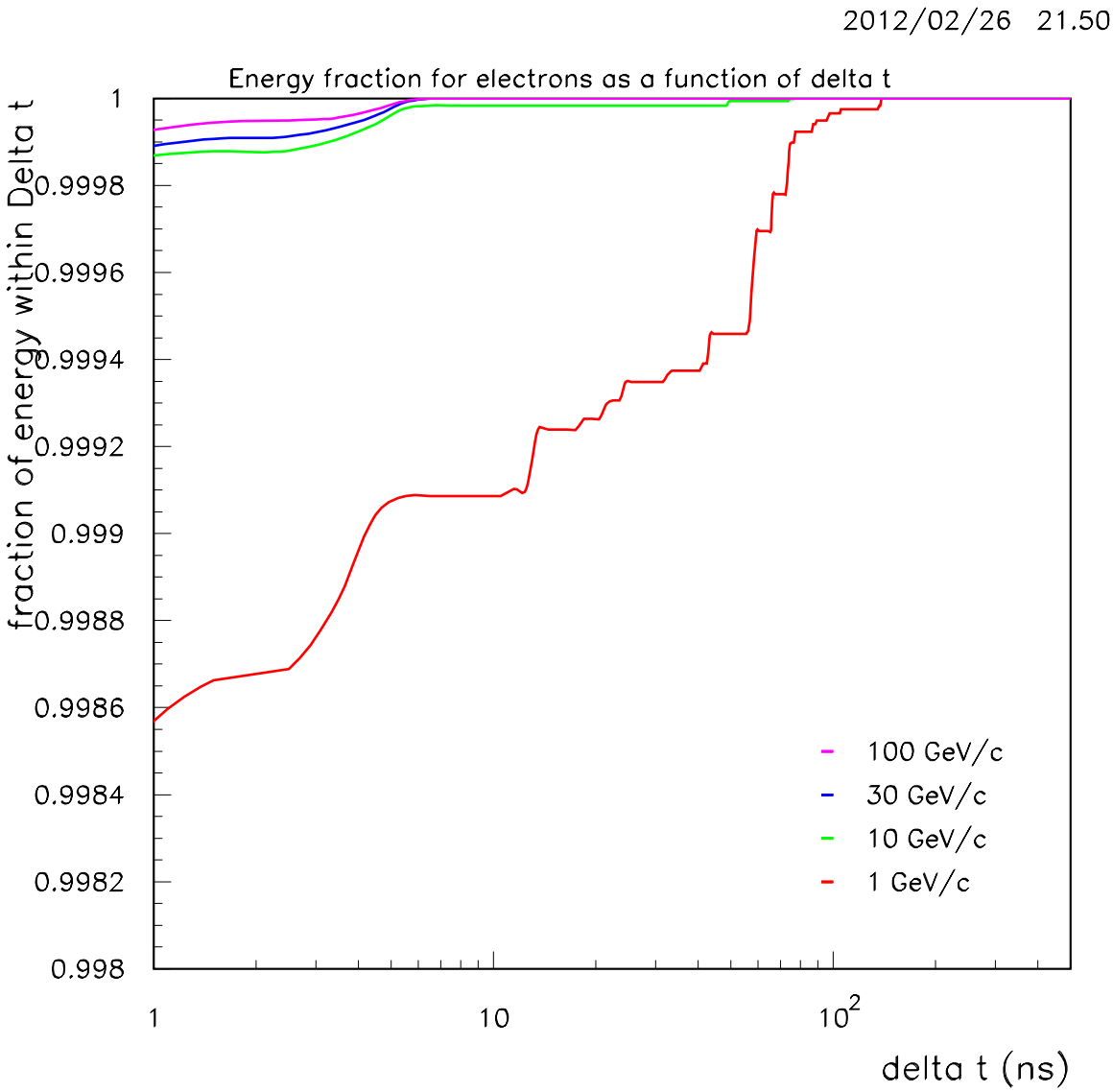

Figure 19. Fraction of energy within δt vs δt for electrons of 1 GeV/c, 10 GeV/c, 30 GeV/c and 100 GeV/c momentum. Note the suppressed zero on the y axis.

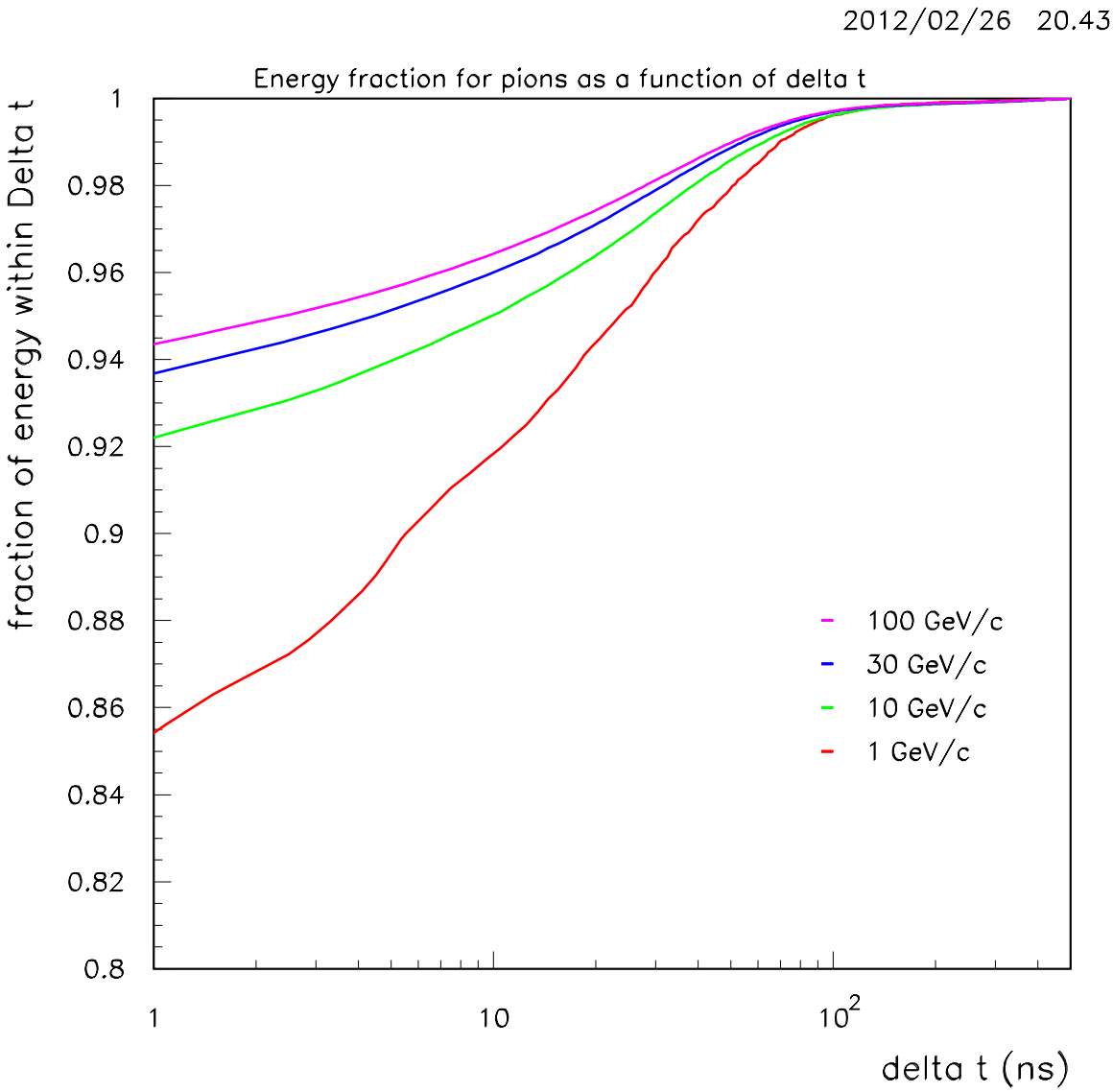

Figure 20. Fraction of energy within δt vs δt for pions of 1 GeV/c, 10 GeV/c, 30 GeV/c and 100 GeV/c momentum. Note the suppressed zero on the y axis.

6. Why does the Calorimeter Work with the traveling gate trigger?

Let us take the case of a non-interacting particle of velocity β traveling in a calorimeter medium. Let us say that it goes out of the traveling gate of g ns, after traveling a distance d and time t. Then at that point, $t_{light} = d/c$, $t = \frac{d}{\beta c}$ and g = t - t_{light}. This leads to the equations $d = \frac{\beta\, g\, c}{1-\beta}$ and $t = \frac{\beta}{1-\beta}$. Figure 21 shows the distance d as a function of β and Figure 22 shows the time t as a function of β for gate times of 1 and 2 ns. As $\beta \rightarrow 1$, both d ans t reach large values since the speed of the particle approaches that of light. For $\beta \rightarrow 0$, the $t \rightarrow g$. So one might ask, why don't the slower particles go out of the gate before their energy gets measured by the calorimeter? Why does the traveling gate trigger work at all? The answer in a nutshell is that dE/dx forces in calorimetric materials are very powerful and decelerate the particle faster than the time taken for it to go out of the gate. Most of the particles are above the Bragg peak (for a pion this occurs at a kinetic energy of $\approx$ 10 keV). The more a particle slows down the greater the dE/dx forces on it. So it decelerates at a greater and greater rate till it stops.

To show this we examine dE/dx as a function of β for a variety of materials as shown in Figure 23. The curves are calculated using the Bethe-Bloch formalism for large β and using the Andersen-Ziegler formalism [8] for smaller values of β, well below the Bragg peak. Figure 23 shows the dE/dx curves for a variety of materials ranging from tritium gas to tungsten. We can use these curves to calculate the range of particles such as pions, protons and deuterons that are the result of hadrons interacting in the calorimeter. Figure 24 shows the range of pions as a function of the pion kinetic energy in various calorimetric materials ranging from liquid helium (least stopping power) to tungsten (greatest stopping power). Superimposed are the functions d at which a particle goes out of the time gate for gates of 1 and 2 ns. It can be seen that the range in all the calorimetric materials considered is smaller than the function d except for liquid helium and that too for a small range of kinetic energy. Figure 25 shows the corresponding functions for a proton as a function of the kinetic energy of the proton. Again, except for liquid helium, all other calorimetric materials shown have no trouble stopping the proton before it runs out of the traveling gate. Figure 26 shows the corresponding plots for a deuteron as a function of the deuteron kinetic energy. Deuterons also will fall out of the gate earlier in liquid helium but all deuterons can be accommodated for a gate of 2 ns for the other calorimetric materials. If the gate of 1 ns is used, one experiences some difficulty for deuterons in the kinetic energy range 200 MeV to 6 GeV for calorimetric materials such as aluminum and carbon. Copper, iron and tungsten do well for all deuteron energies for both gates. We can also look at the above behavior in terms of the time taken for the particle to range out as a function of the kinetic energy of the particle. Figure 27 shows the range-out time in ns vs kinetic energy of the pion for various calorimetric materials. Superimposed is the time taken for the pion to fall out of the gate g for g=1 and 2 ns as a function of the kinetic energy of the pion. The results are the same as shown in Figure 24 except that we are looking at the problem in the time domain.

6.1. Interactions

In the above discussion, we have shown that dE/dx is a sufficiently strong force to bring charged particles to a stop before they fall outside the traveling gate. If the charged hadron interacts before it comes to a complete halt and produces secondary charged hadrons, all the secondaries will have shorter range than the remaining range of the primary hadron, since they will have lower momenta than the interacting hadron. However, the interaction can also produce neutral particles (neutrons, K-zeros and lambdas) which do not undergo dE/dx range out and can produce hits that may fall outside the gate. We have estimated these effects in Figure 20 and find them to be small.

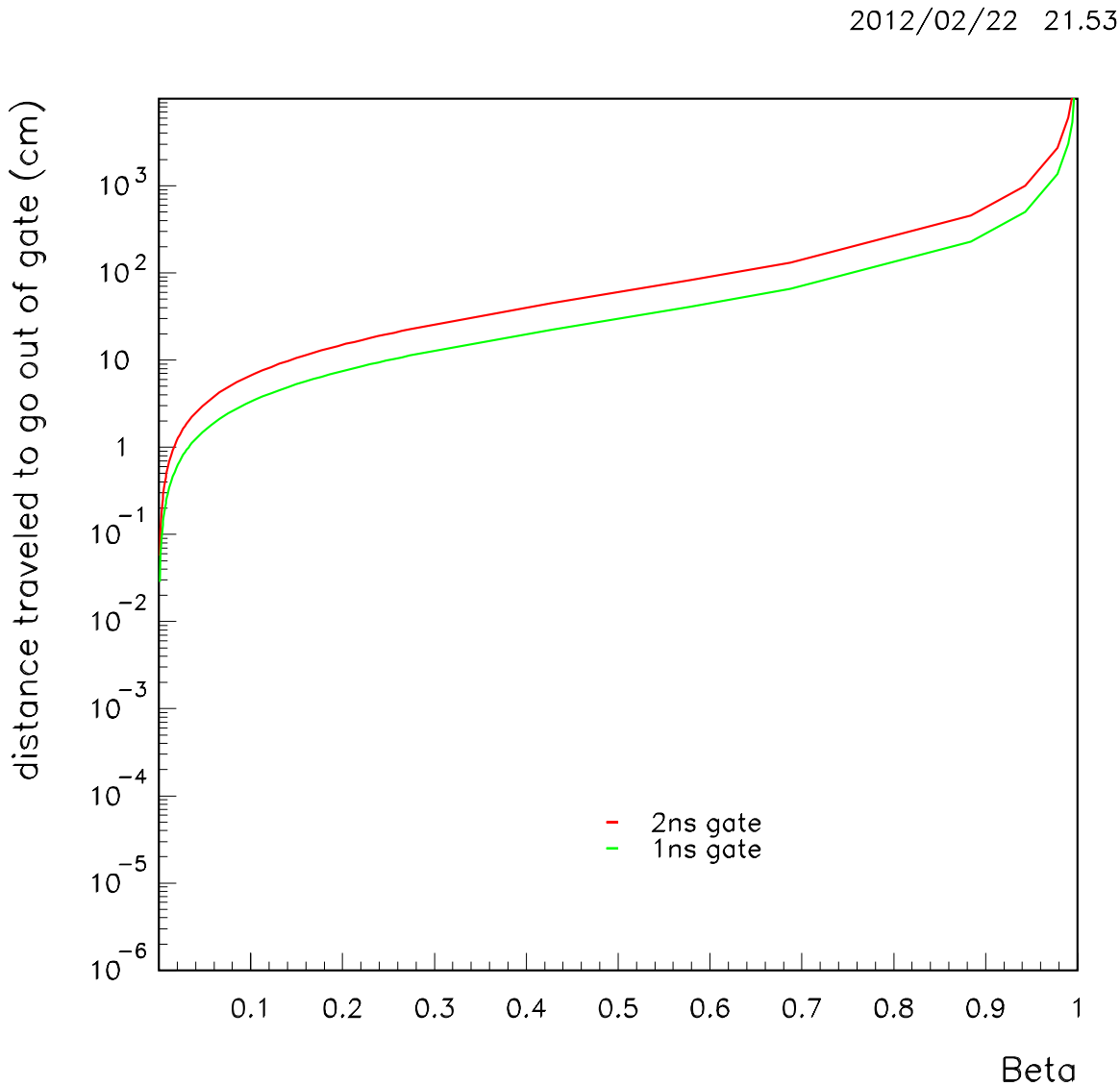

Figure 21. The distance traveled by a particle of velocity βc before it goes out of the traveling gate trigger for gates of 1 ns and 2 ns.

6.2. Tracking dimension considerations

In the above discussion, we have assumed that the particle starts out traveling in the calorimetric medium to simplify the discussion. However, in our simulation, the tracking volume extends to 80 cm radius at which point the calorimeter begins. For a gate $g = 2\ ns$, and a calorimeter inner radius of 80 cm, the $\beta_{transverse}$ of the particle has to be greater than 0.572 for it to be in gate before it reaches the calorimeter. This corresponds to a kinetic energy of 30 MeV for a pion and 205 MeV for a proton with zero longitudinal momentum. These particles have ranges of 0.8 cm and 4 cm in iron respectively. If one wants to accept particles of lower momentum, it may be worth increasing the gate to 10 ns (say) for the first 10 cm of the calorimeter layers. This will permit 3 MeV pions and 20 MeV protons to be accepted. One has of course to pay the price in

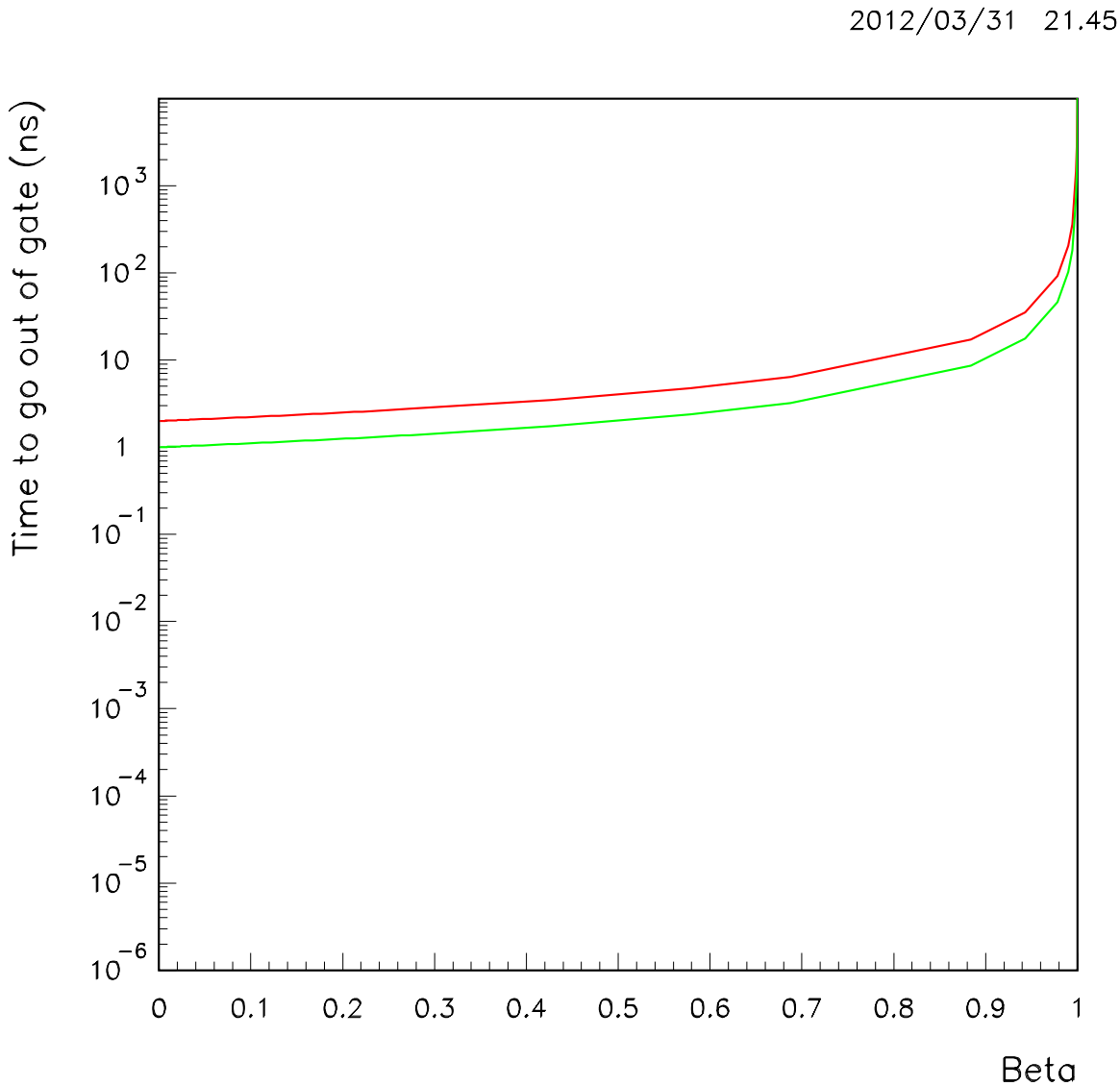

Figure 22. The elapsed time traveled by a particle of velocity βc before it goes out of the traveling gate trigger for gates of 1 ns and 2 ns.

background rejection to accommodate the longer gate. These numbers are given here to frame the problem and its solution. The optimization of the trigger has to be done with a full Monte Carlo accommodating the transverse and longitudinal momenta of the particle concerned and the background levels tolerable.

6.3. Pixel size

We have also done a preliminary study to investigate the optimal pixel size for the calorimeter. The electron showers have a much higher hit density than the hadronic tracks, and the chances of two tracks hitting the same pixel is highest for electron showers. Figure 28 shows the ratio of total number of pixels hit/total number of Geant3 hits for a beam of 1000 electrons of energy 10

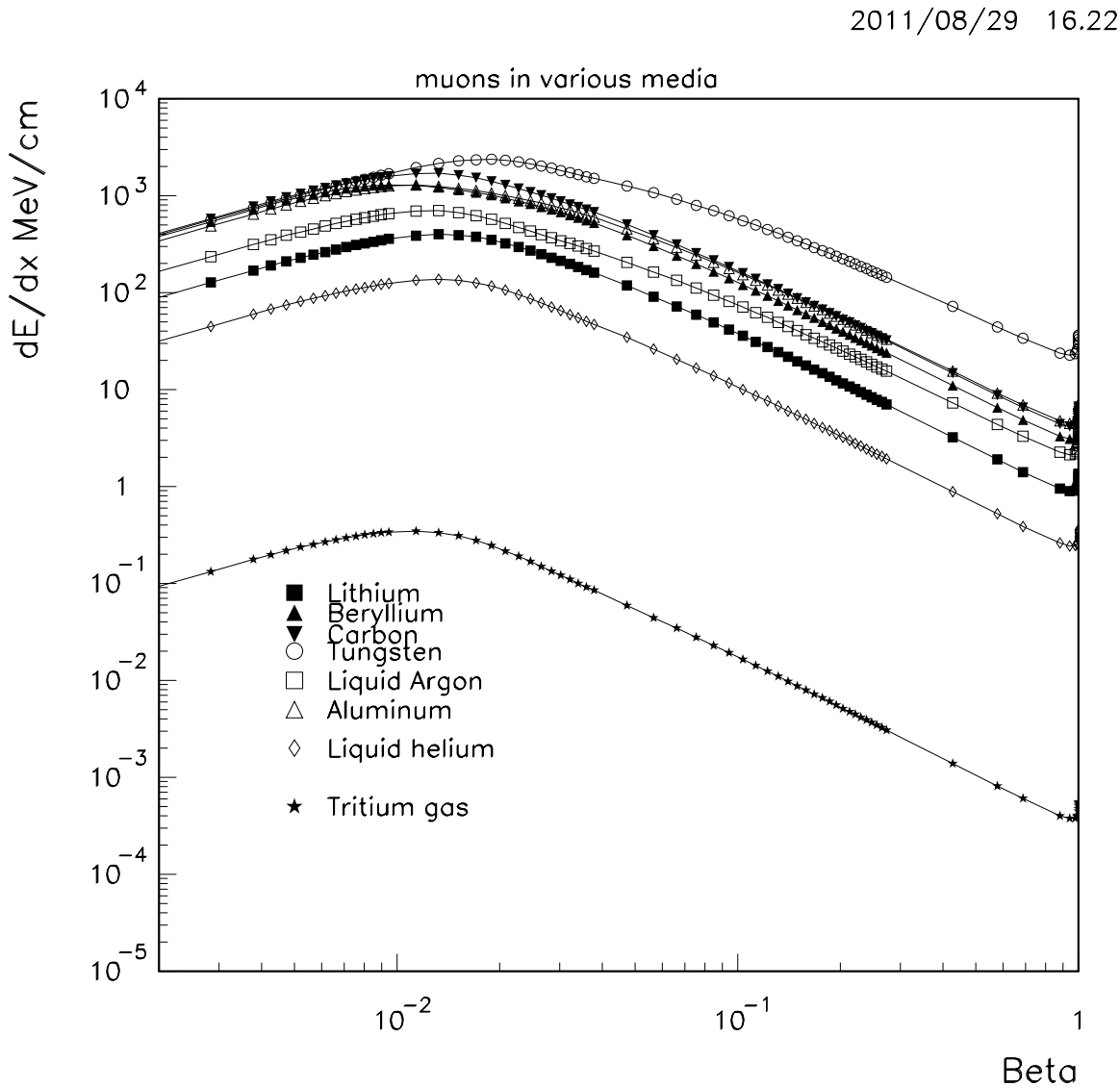

Figure 23. dE/dx distributions as a function of β for a variety of materials. Both the Bethe-Bloch and Andersen-Ziegler formalisms are used in deriving these curves.

GeV, 30 GeV and 100 GeV. Due to resolution effects, the number of hits fluctuate largest for the lowest momentum, hence the plots are widest for the lowest momentum (10 GeV). But the mean value of the ratio pixel hit/total hit is the same for all beam momenta. The hit density is highest for 100 GeV. The fact that the mean value of the ratio is independent of energy implies that the shower dynamics plays a greater role in determining this parameter rather than the shower density. Photons converting near the edge of the iron absorber will likely produce an electron and a positron in the appropriate pixel, no matter what the pixel size (to first order). More studies need to be done as a function of pixel size to optimize this. This multiple hit problem can be corrected for by using a small additional calibration constant, which seems to be independent of the shower energy. Pixel thickness needs to be adjusted so that there is enough signal to fire

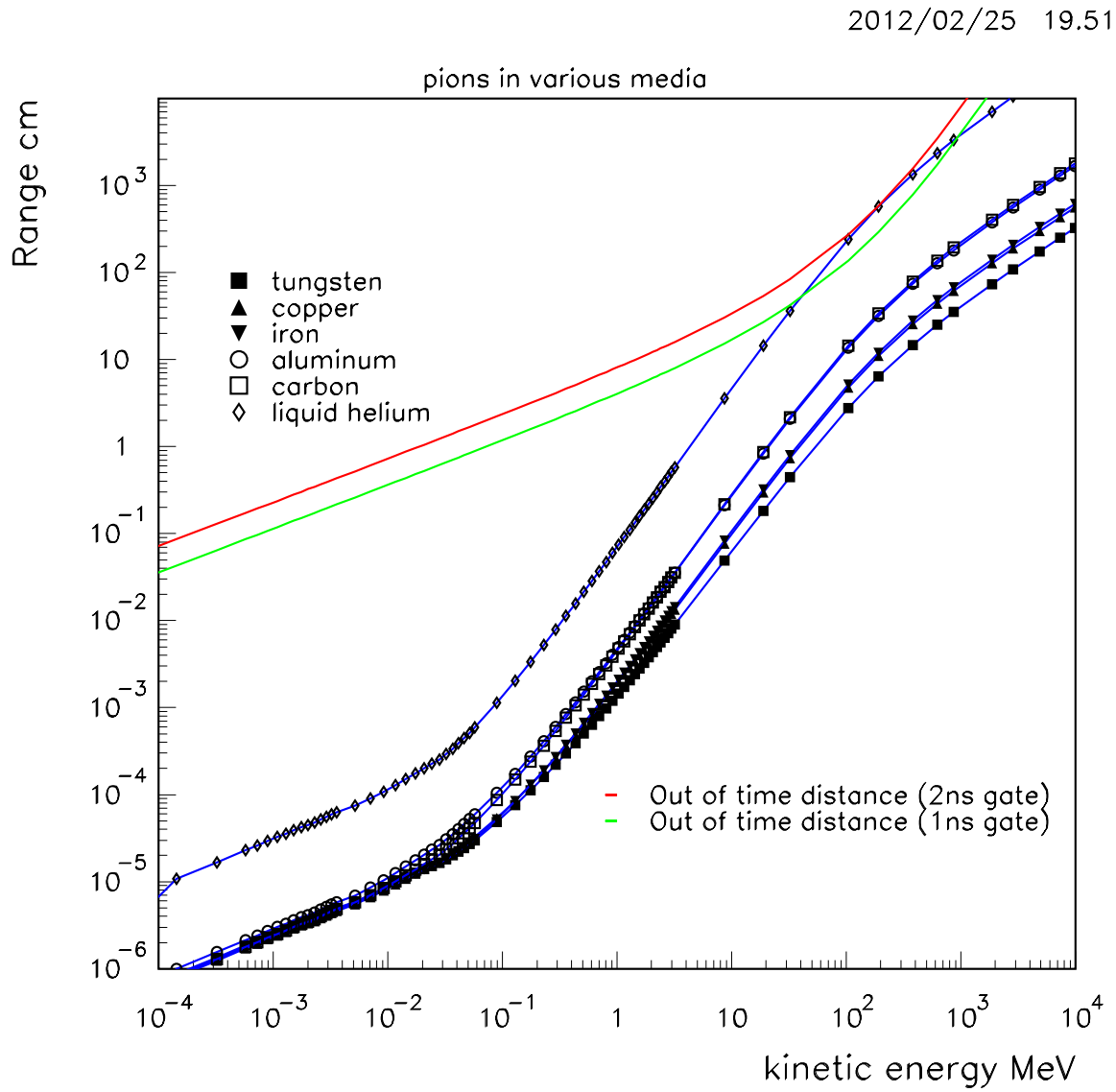

Figure 24. Range as a function of kinetic energy of pions for a variety of calorimetric materials. Superimposed is the distance that would be traveled by the pion before it falls out of gate.

pixel for a minimum ionizing track. The pixel area is connected with the capacitance of the system and the ability to trigger the pixel with a 2 ns gate. These optimizations have to be performed in subsequent studies.

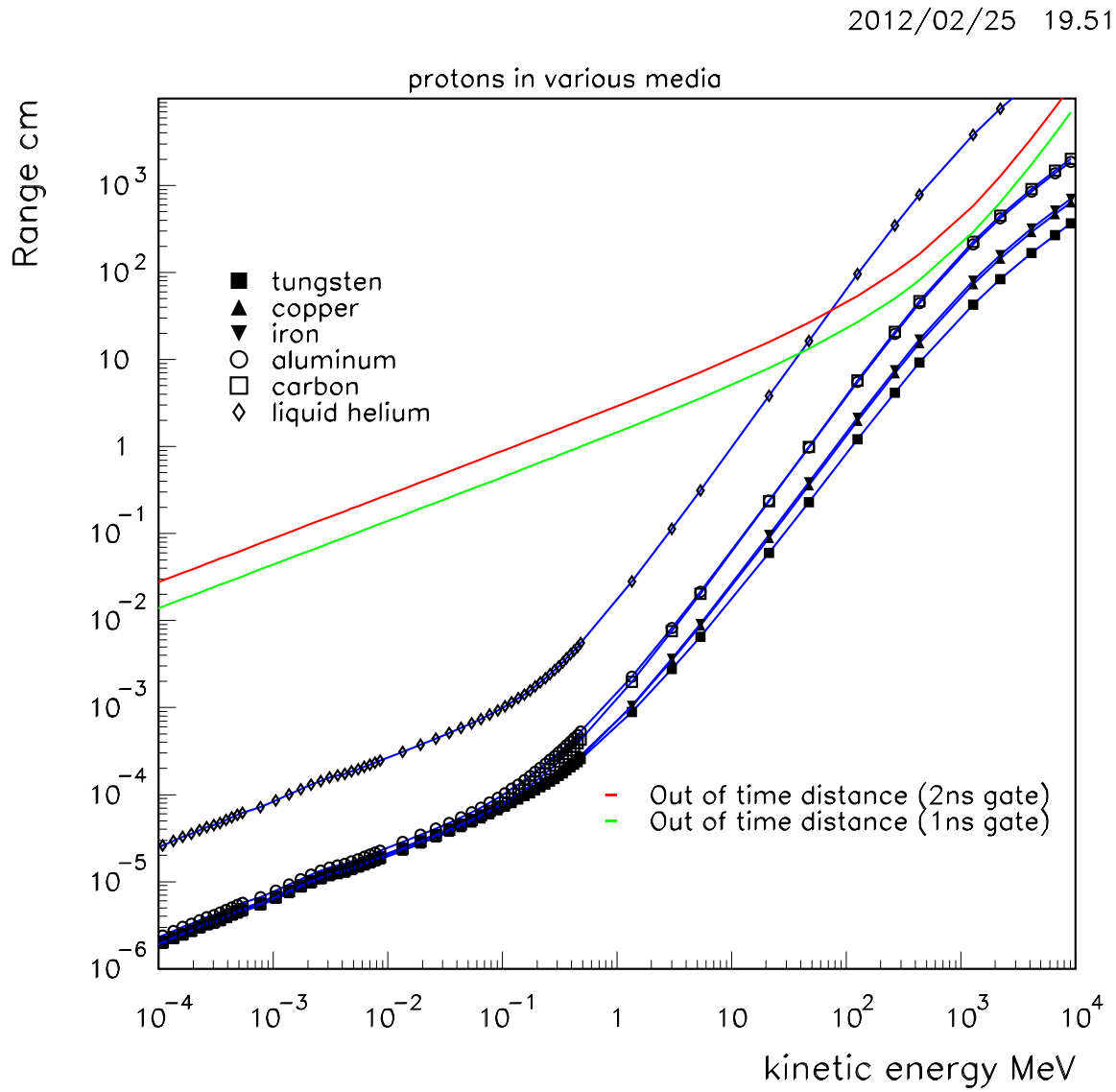

Figure 25. Range as a function of kinetic energy of protons for a variety of calorimetric materials. Superimposed is the distance that would be traveled by the proton before it falls out of gate.

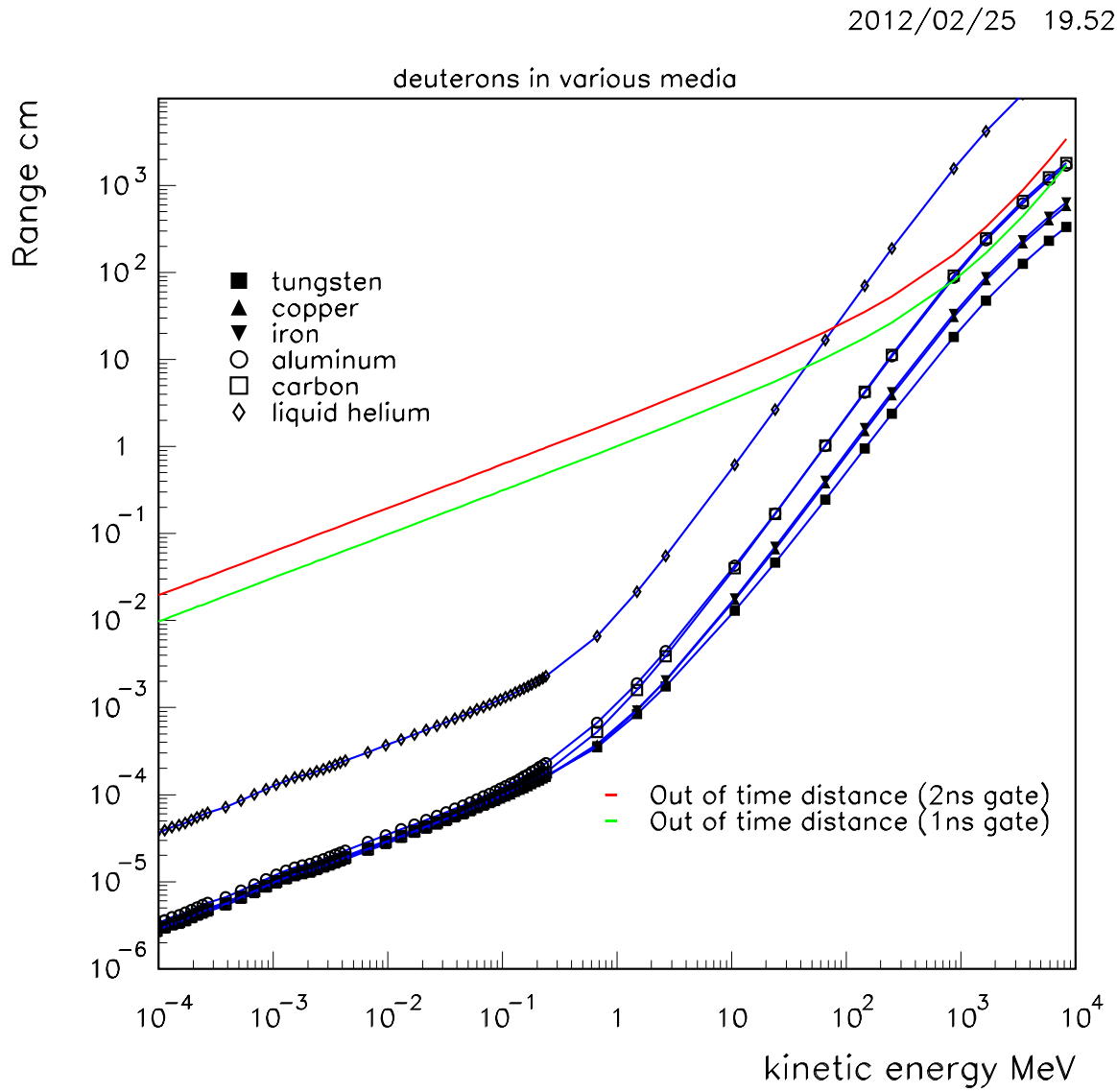

Figure 26. Range as a function of kinetic energy of deuterons for a variety of calorimetric materials. Superimposed is the distance that would be traveled by the deuteron before it falls out of gate.

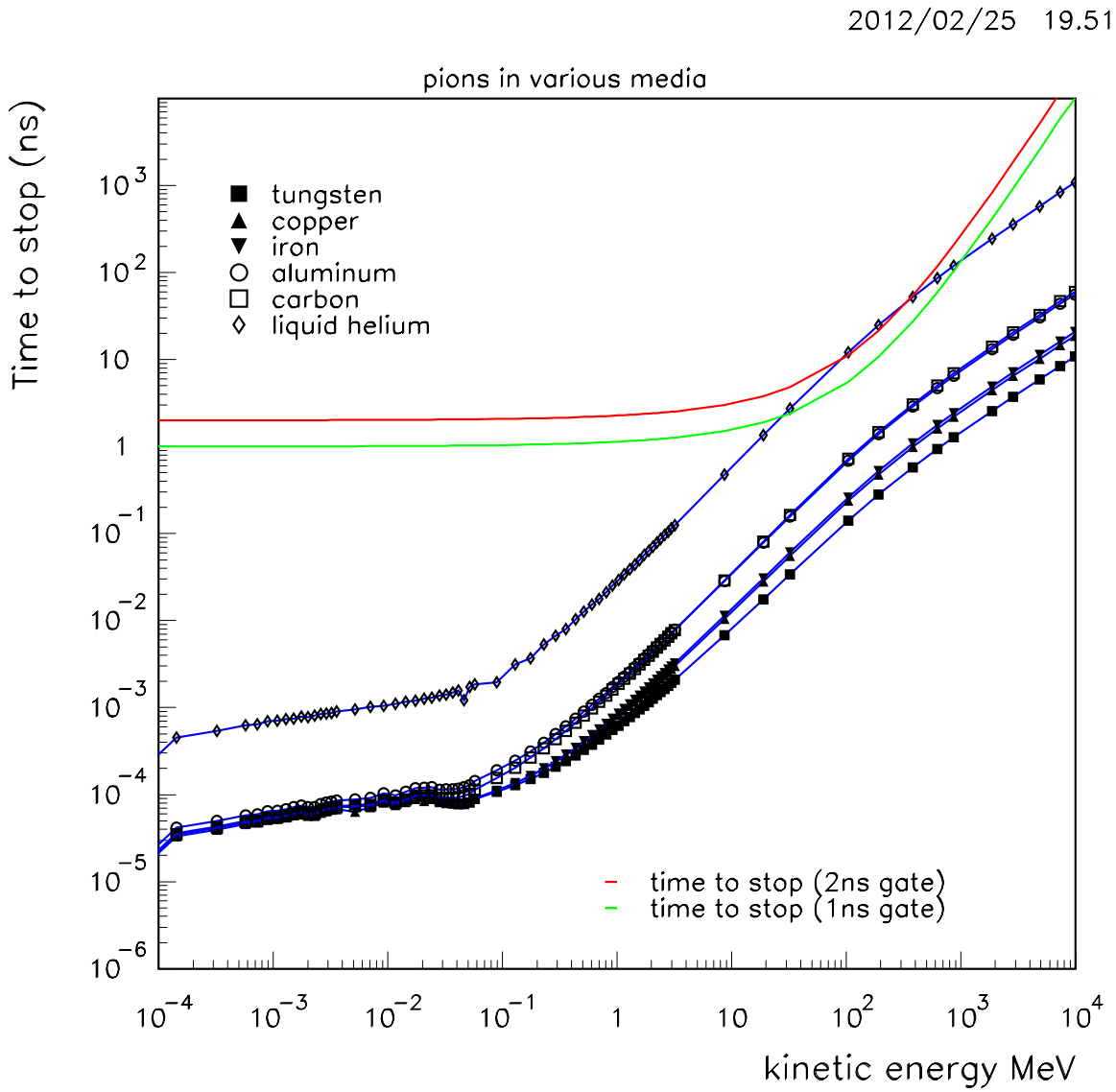

Figure 27. Time taken before it comes to a stop as a function of kinetic energy of pions for a variety of calorimetric materials. Superimposed is the time that would be traveled by the pion before it falls out of gate.

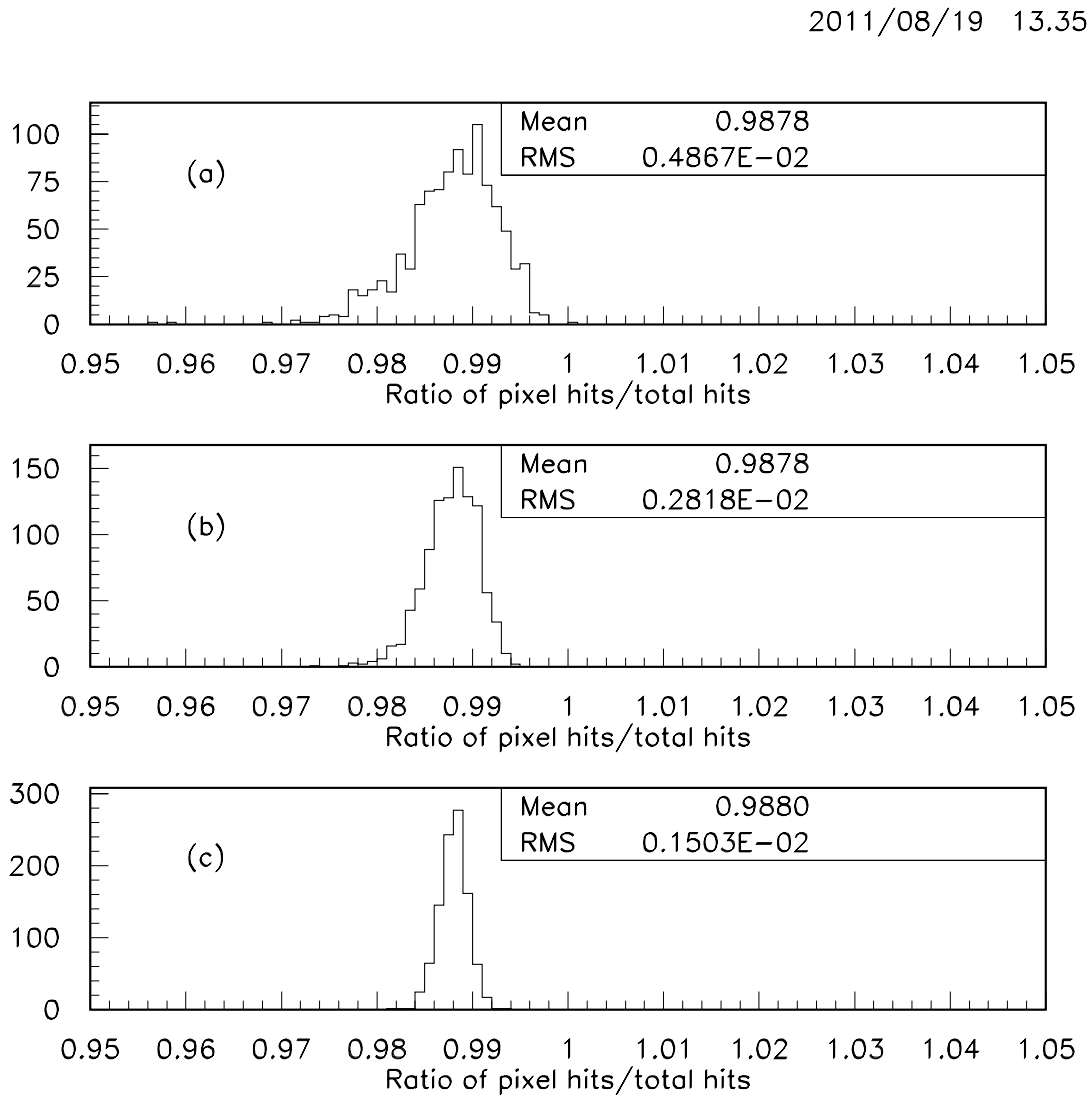

Figure 28. Ratio of number of hits in a pixel calorimeter with 200 microns linear pixel dimension/total number of hits as a function of beam energy for electrons. (a) is for 10 GeV electrons, (b) is for 30 GeV electrons and (c) 100 GeV electrons.

7. Compensation Schemes

The mechanism of energy loss in hadronic showers in calorimeters is now well understood [9]. As hadrons from the shower interact and produce more particles, kinetic energy is spent in breaking up the nuclei in the calorimeter as well as giving energy to spallation neutrons which travel far and do not give up all their energy as dE/dx within the allowed trigger gate of the calorimeter. Electromagnetic showers do not suffer from this loss of energy since nuclear breakups occur extremely rarely in EM showers. Electromagnetic showers thus manifest all their energy as dE/dx hits in the calorimeter. This results in the well known e/π ratio that is greater than unity that is a characteristic of the calorimeter. Left uncorrected (uncompensated), this e/π ratio results in an increase in the calorimeter resolution. The resolution function of a calorimeter is parametrized as $\sigma/E = C \oplus S/\sqrt(E) \oplus N/E$, where $\oplus$ implies addition in quadrature. The N coefficient is due to noise in the calorimeter, the S coefficient is due to sampling fluctuations and C term is referred to as the constant term is due to individual calibration errors between digitizing cells as well as due to an e/π ratio different from unity. At high energies, the constant term comes to dominate calorimetric resolution and it is in everyone's interest to produce a calorimeter with a negligible constant term. Lack of compensation also produces non-linear responses in the calorimeter since the fraction of a shower that is electromagnetic increases with shower energy. This is because EM showers do not further produce hadrons whereas hadronic interactions produce EM showers by π^0 production. This increase in EM fraction as a function of shower energy will cause a non-linear response to the shower by the calorimeter.

The calorimeter resolution function can be characterised by

$$\frac{\sigma_{E_{live}}}{E_{live}} = \frac{\sigma_{E_{ideal}}}{E_{ideal}} \oplus \sigma_\lambda < \frac{(1-f)}{1-\lambda(1-f)} > \tag{6}$$

where $f = e/pi$ ratio, λ is the fraction of hadronic energy per event. It can be seen that when $f \rightarrow 1$, the constant term vanishes.

Compensation techniques can be broadly characterized into two types- hardware and software compensation.

7.1. Hardware Compensation

The spallation neutrons can be used to re-interact with hydrogen atoms in the calorimetric readout medium which will cause slow knock-on protons to deposit energy in the calorimetric medium. The protons are close to their Bragg peak and deposit much more energy per distance traversed than a minimum ionizing particle. If the calorimeter readout consists of ADC's then this energy can be measured and the amount of hydrogenous material tuned to compensate for the hadronic energy loss [10]. Since we do not employ ADC's and only use digital information, this method of compensation is not possible in a purely digital calorimeter.

Another form of hardware compensation is the dual readout calorimeter [11] where two types of readout digitize a different mixture of scintillation and Cherenkov light from the shower. Since these two outputs have different sensitivities to hadronic and electromagnetic tracks, they can be used to compensate for the hadronic energy loss.

7.2. Software Compensation

7.2.1. Separating EM hits and Hadronic Hits In calorimeters with a high degree of granularity, it is possible to distinguish between hadronic tracks and EM shower tracks by the density of hits in heir neighborhood. Figure 10 shows this effect, the density of hits being much greater in the EM shower due to $\pi^0 s$ than near the hadronic tracks. We will assume in what follows that if it is possible to pattern recognize an effect by eye, it is possible to write a pattern recognition program to perform the same task. The latter requires many years of effort and will require

dedicated FTE's of effort to achieve. We can however examine the feasibility of the algorithm by using the Monte Carlo information to separate EM and hadronic hits in the calorimeter.

Assuming a perfect separation between EM and hadronic hits, we put the calorimeter in a test beam setting in the Monte Carlo and employ beams of 10 GeV, 30 GeV and 100 GeV pions. For each event, we have two variables to compute the energy of the shower - the total number of EM pixel hits and the total number of hadronic pixel hits. We employ two calibration constants one for EM hits and one for hadronic hits and minimize the least square resolution between the beam energy and the digitized energy to obtain the two calibration constants.

7.3. Vertex Counting technique

The dE/dx deposited by hadronic tracks and those deposited by EM tracks are very nearly the same provided the hadronic track is close to minimum ionizing. The difference is in the energy lost during nuclear interactions. In the software compensation technique separating EM and hadron hits, where one assumes different calibration constants for EM hits and hadronic hits, one is essentially trying to estimate the number of hadronic nuclear interactions based on the number of hadronic hits. The digital calorimeter described here has the ability to count the number of hadronic vertices using pattern recognition. One can use the number of vertices in an event to directly estimate the missing hadronic energy. One then assumes the same calibration constant for hadronic and EM hits but has an extra variable in the event– the number of hadronic vertices. The calibration constants associated with the hits and the number of vertices are again determined using a least squares minimization technique.

In practice, to make this method work, one will have to write pattern recognition algorithms to determine the number of hadronic vertices. However, we can investigate the feasibility of this method using information provided by Geant3. We decided on three different criteria to select hadronic vertices.

- Cut 1 –Number of hadronic vertices that occur on a charged track
- Cut 2 – Vertices from Cut 1 with the additional requirement that the kinetic energy lost per vertex is > 0.1 GeV
- Cut 3 – Cut 2 vertices with more than one outgoing charged track.

These are criteria arrived at to get a sample of hadronic vertices. Cut 2 showed us that kinetic energy is lost at vertices where the hadron stops in the calorimeter without any outgoing tracks. Figure 29 is a picture of a 100 GeV pion shower on which are shown Cut 2 hadronic vertices as yellow crosses. One needs to count not only the hadronic interactions but also hadronic stopping vertices.

Figure 30 shows the missing energy per hadronic event vs the number of vertices for an ensemble of 1000 pions of energy (a) 1 GeV (b) 10 GeV (c) 30 GeV and (d) 100 GeV. A clear correlation is evident between the number of vertices and the missing energy. We use Cut 2 vertices for this plot. The other vertex selections show similar behavior. Figure 31 shows the linearity of the mean number of vertices per event as a function of the pion energy for vertices chosen by cuts 1,2 and 3. All three selections show excellent linearity. Both the linearity as well as the proportionality between the number of vertices and missing hadronic energy are necessary for the number of vertices being used as a calibration variable, since one does not want the calibration constants to depend on pion energy.

7.4. Calorimeter Performance Plots

We use the two compensation techniques outlined above as well as the uncompensated calorimeter output to study the characteristics of the calorimeter. Figure 32 shows the e/π ratio for pions as a function of momentum with and without compensation and with and without the traveling gate cut. The uncompensated time cut sample has the largest e/π ratio followed

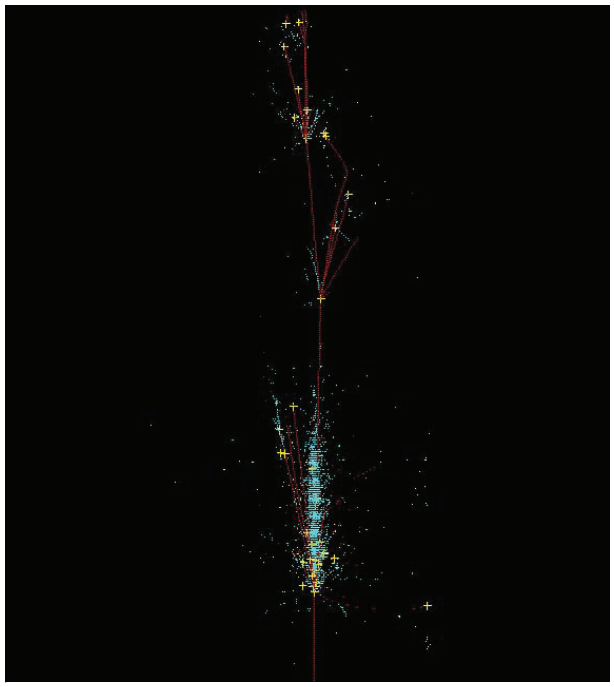

Figure 29. Vertices (yellow crosses) in a 100 GeV pion shower obtained using cut2.

by the uncompensated sample without the time cut. Both compensation techniques yield e/π ratios close to unity with and without time cut, indicating that the compensation least squares algorithm was successful in this regard. Figure 33 shows the resolution function σ/E for pions as a function of momentum with and without compensation and with and without the traveling gate time cut. As a rule, the time cut worsens the resolution somewhat. Software compensation using the hadron EM hit separation technique significantly improves the calorimeter resolution. The vertex counting method give significantly better resolution still than the hadron/EM separation method and this is due to the fact the number of vertices is a direct measure of the energy loss in the shower. In practice, one can experiment with more sophisticated vertex counting algorithms where one can have the energy lost at a vertex be proportional to the number of charged tracks at the vertex and see if such models improve resolution further. Also, both compensation techniques, especially the vertex counting technique is immediately applicable to high resolution calorimeters such as the liquid argon TPC [12].

Figure 34 shows the function $\sigma/\sqrt{(E)}$ as a function of pion momentum. The uncompensated functions show significant non-flatness with pion momentum indicating a significant constant term in the resolution function. The compensated resolution functions are flat with momentum indicating negligible constant terms. The vertex counting technique again displays superior performance over the EM/hadron separation technique.

The electron resolution can be obtained by taking the square root of the number of hits in this digital calorimeter. The calibration constant for electrons is 0.8676×10^{-2} GeV/hit, or 115.26 hits/GeV. This works out to σ/E of 9.31%. It may be possible to improve this using correlations in the shower and using weights rather than sampling fractions [13].

7.5. Compensation and time resolution of the calorimeter

In Figure 34, it can be seen that it is possible to get a near-optimal resolution for compensated calorimetry with a gate as little as 2 ns. This is because the e/pi ratio is close to one. Whereas for an uncompensated calorimeter, one needs to wait for $\approx$ 100-150 ns for the delayed signal to

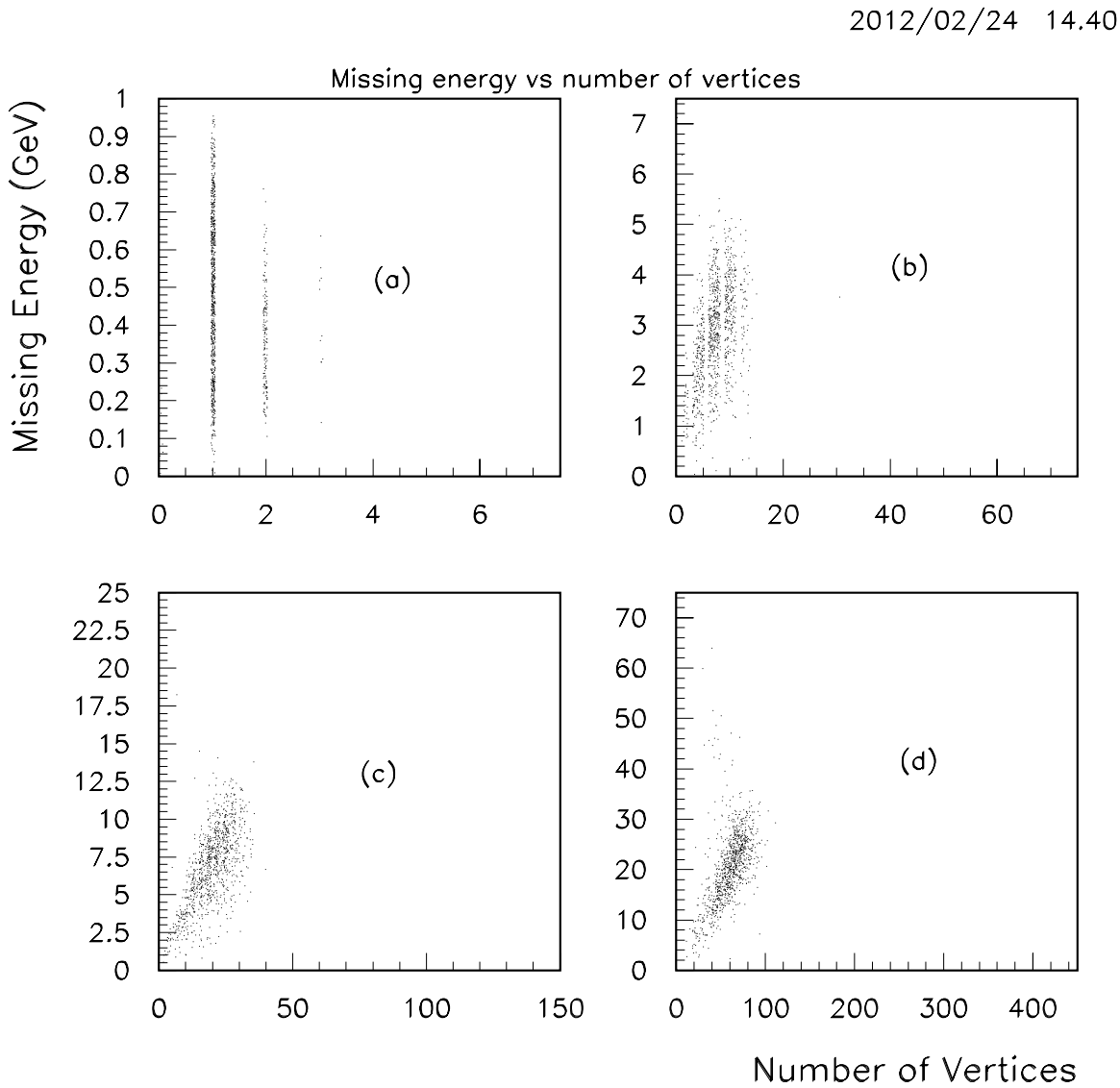

Figure 30. Missing hadronic energy in event vs number of vertices as a function of pion energies of (a) 1 GeV (b) 10 GeV (c) 30 GeV and (c) 100 GeV. It can be seen that event to event there exists strong correlation between missing hadronic energy and number of hadronic vertices. We use cut 2 for the vertices in this plot.

collect and even then one does not obtain optimal resolution. This is important for experiments in CLIC where the difference between 2 ns and 150 ns can make a lot of difference in background from neighboring interactions.

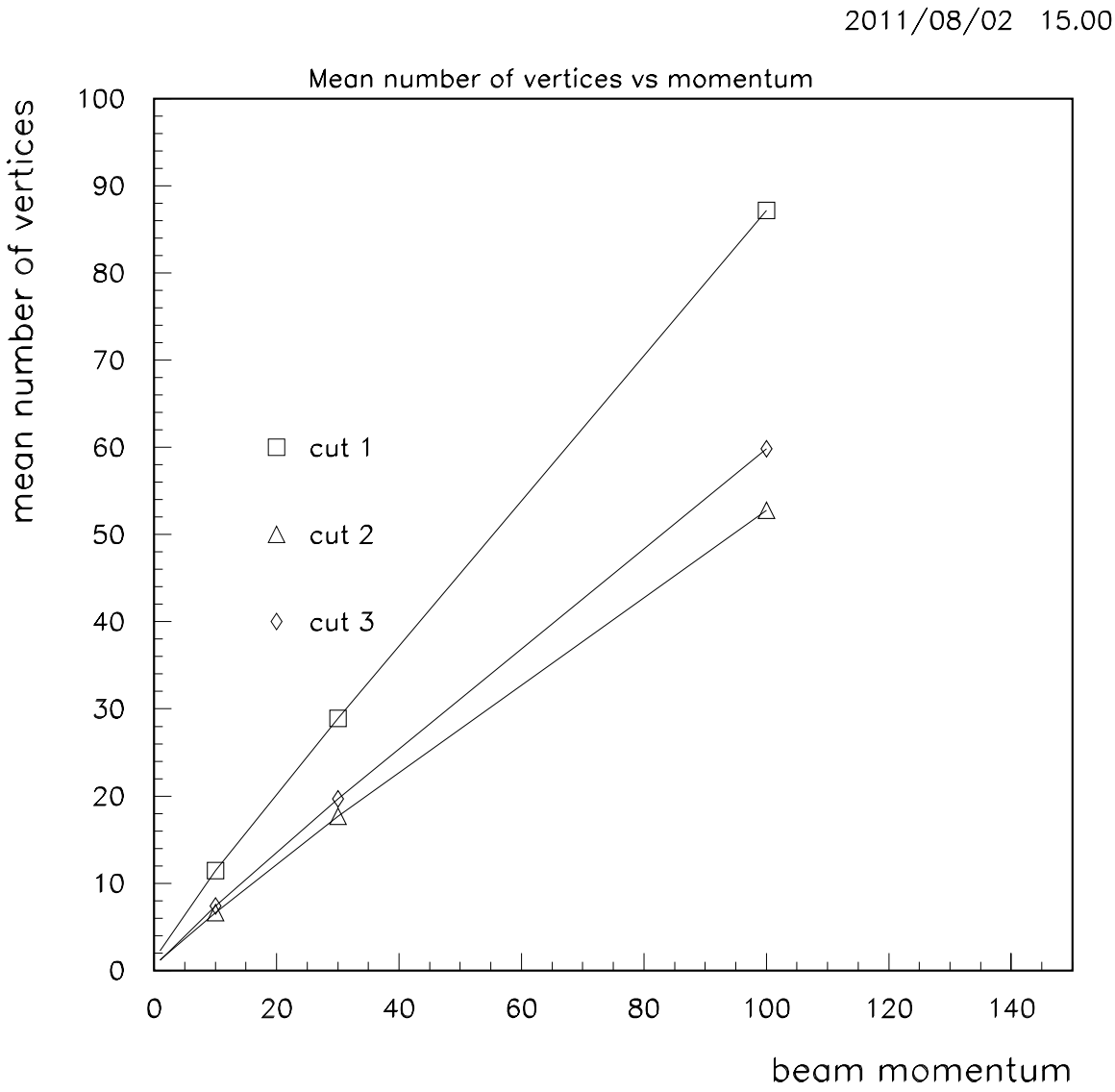

Figure 31. Linearity of mean number of vertices as a function of pion beam momentum for hadronic vertices obtained with cut1, cut2 and cut3.

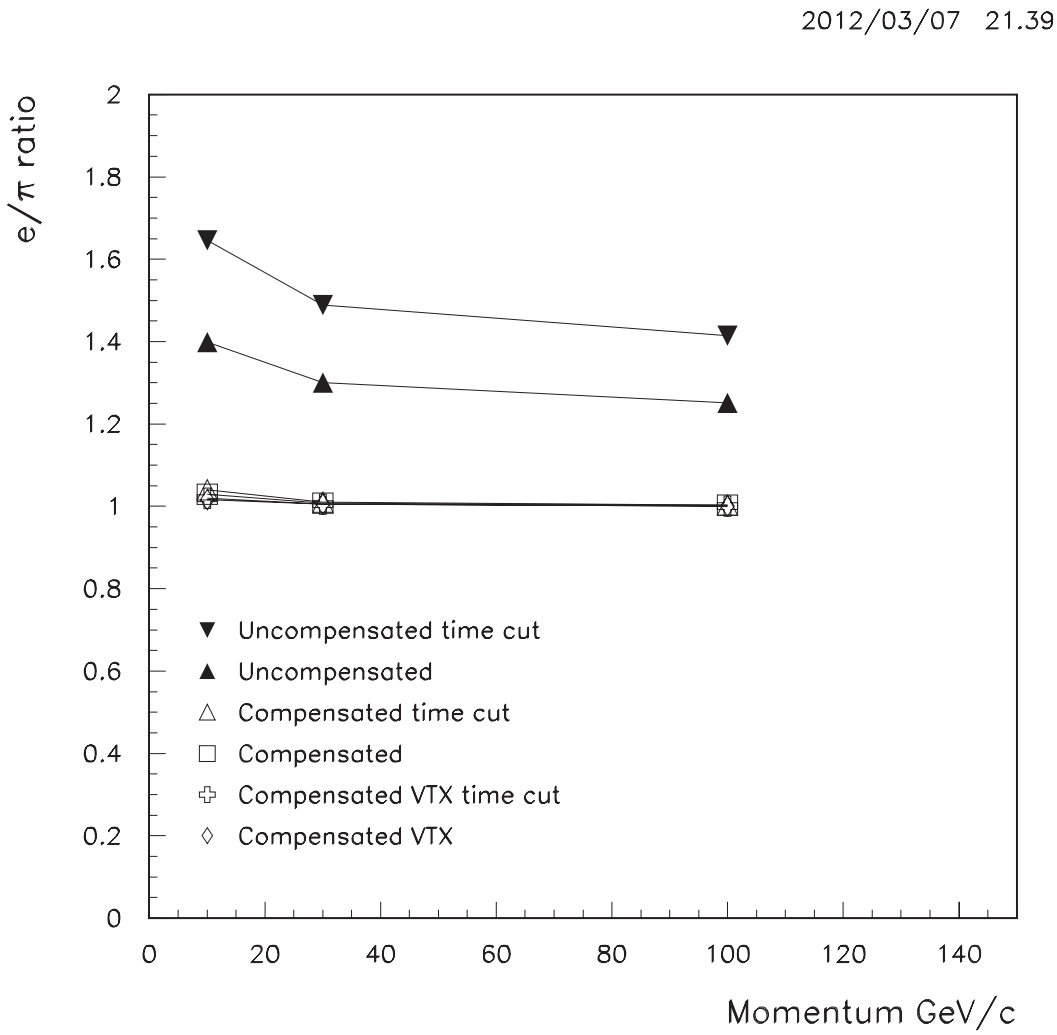

Figure 32. e/π ratio for pions as a function of momentum with and without compensation.

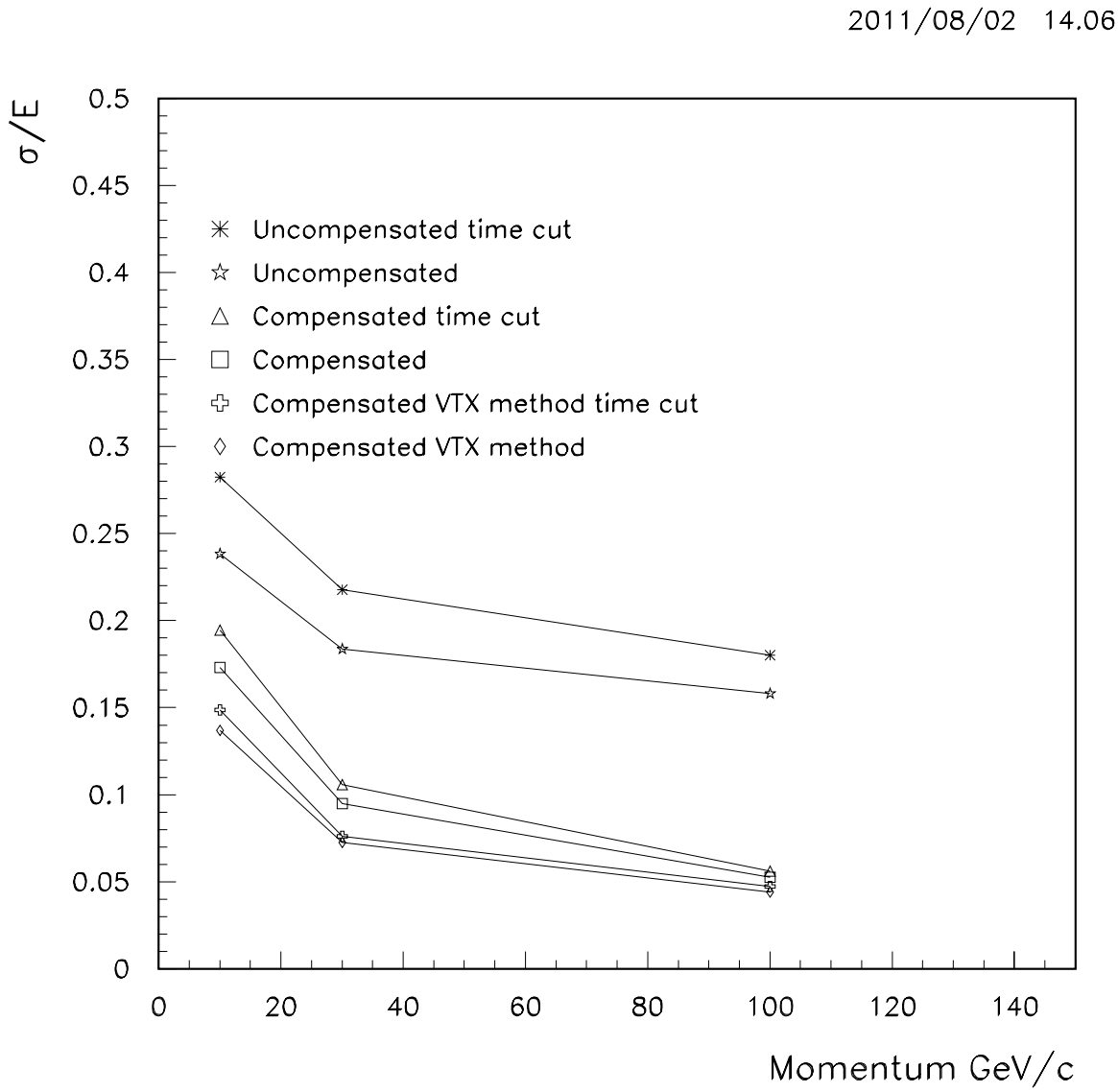

Figure 33. The resolution function σ/E for pions as a function of momentum with and without compensation. It can be seen that the vertex counting algorithm is superior to the EM hit/hadronic hit separation method in compensating.

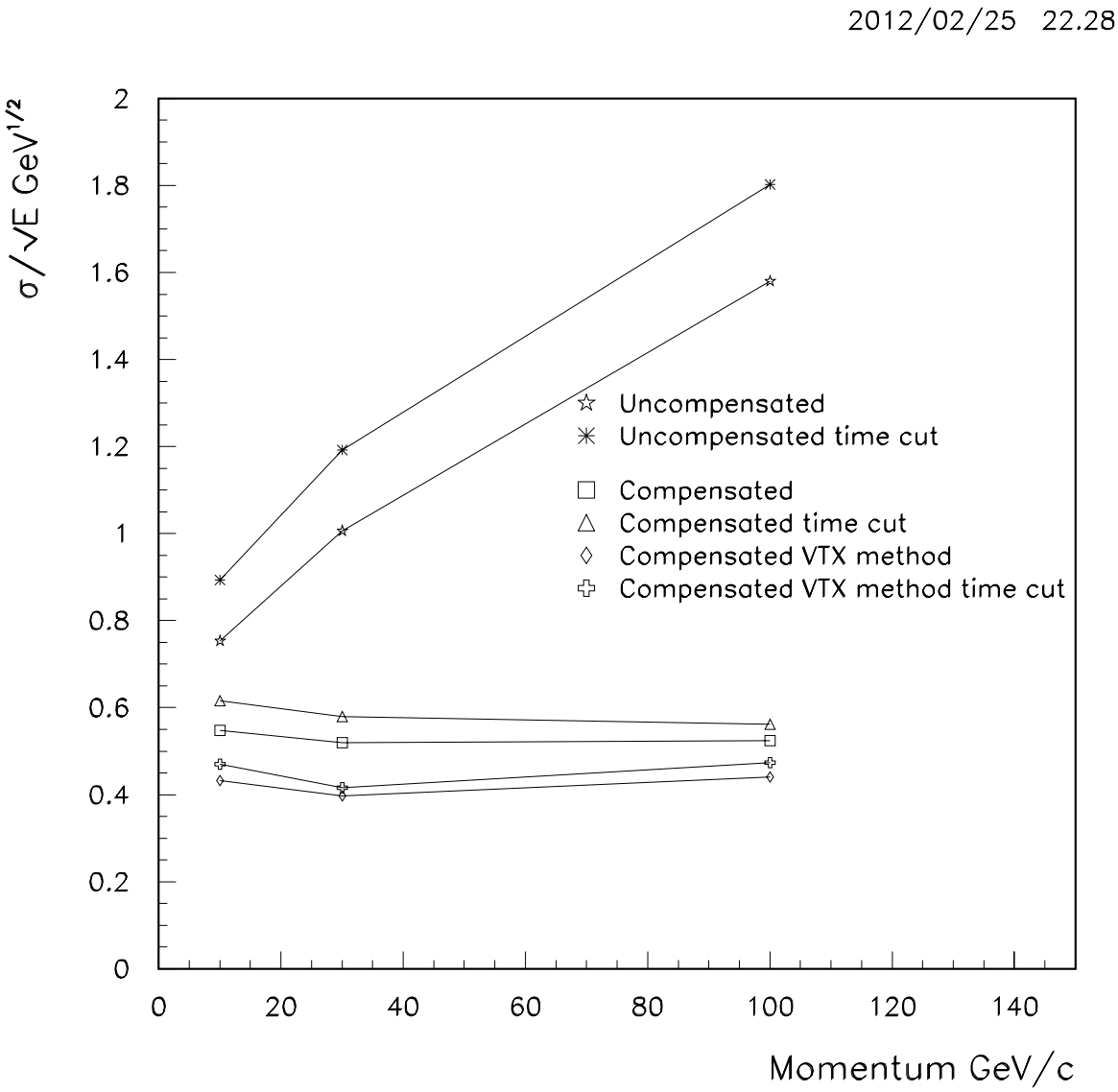

Figure 34. The resolution function $\sigma/\sqrt{(E)}$ for pions as a function of momentum with and without compensation. It can be seen that the vertex counting algorithm is superior to the EM hit/hadronic hit separation method in compensating. After compensation this function exhibits little energy dependence indicating a a negligible constant term in the resolution.

Backgrounds in Tracking Volume			
Particle Type	$\delta t < 2$ **ns**	**In time Hits**	**In time hits/layer**
EM	100282.6	48175.2	2410.
MUONS	7653.7	674.1	33.7
MESONS	53206.2	10654.6	533.
BARYONS	218937.1	22962.7	1150.

Table 3. Background particles in the tracker after timing cuts

8. Remaining Backgrounds in the Tracker

We now proceed to track the particles that survive the cut $\delta t < 2ns$ through our detector model implemented in Geant3. Theorem II now applies and depending on the origin (the MARS vertex), the time of arrival at the origin and the direction of the particles, they can come into the traveling gate trigger in the tracker, travel for some distance and then proceed to move out of time again.

Table 3 shows the backgrounds in the tracking volume as a function of particle type, as total numbers that survive the $\delta t < 2\ ns$ cut, those that then come in time with the gate and the number of in time hits per layer. As can be seen from the hits per layer column, the tracking problem is entirely manageable.

9. Remaining backgrounds in the Calorimeter

The calorimeter is a more challenging problem than the tracking system since it is a more extended volume. We show in this section that the traveling gate trigger coupled with the fine granularity of the pixel system is up to the task of taming the muon collider background.

9.1. EM background

Figure 35 shows the EM particles that survive the $\delta t < 2$ ns cut. The hits shown are unweighted. In practice, there should be a factor of ≈ 20 times more hits. These particles are mostly photons and some electrons and positrons that escape the shielding of the tungsten cone. The EM portion of the calorimeter takes the brunt of these hits as can be seen from the figure. Figure 36 shows the background EM particles that are in time with the traveling gate. These are unweighted hits and in practice there should be ≈ 20 times more hits. However, the hits are considerably less than those in Figure 35.

9.2. Meson background

The meson background consists primarily of charged pions and kaons that are produced in the tungsten cone due to nuclear interactions in EM showers. Figure 37 shows the mesons that survive the $\delta t < 2$ ns cut and Figure 38 shows the mesons that remain in the traveling gate trigger.

9.3. Baryon background

The baryon background consists primarily of slow neutrons and protons that are produced in nuclear interactions associated with the showering of electrons and positrons in the shielding. There are a large number of neutrons in this sample, which interact in the calorimeter and tracker producing knock on protons. Figure 39 shows the baryons that survive the $\delta t < 2\ ns$ cut and figure 40 shows the baryons that are in time with the traveling gate trigger. The hits are unweighted.

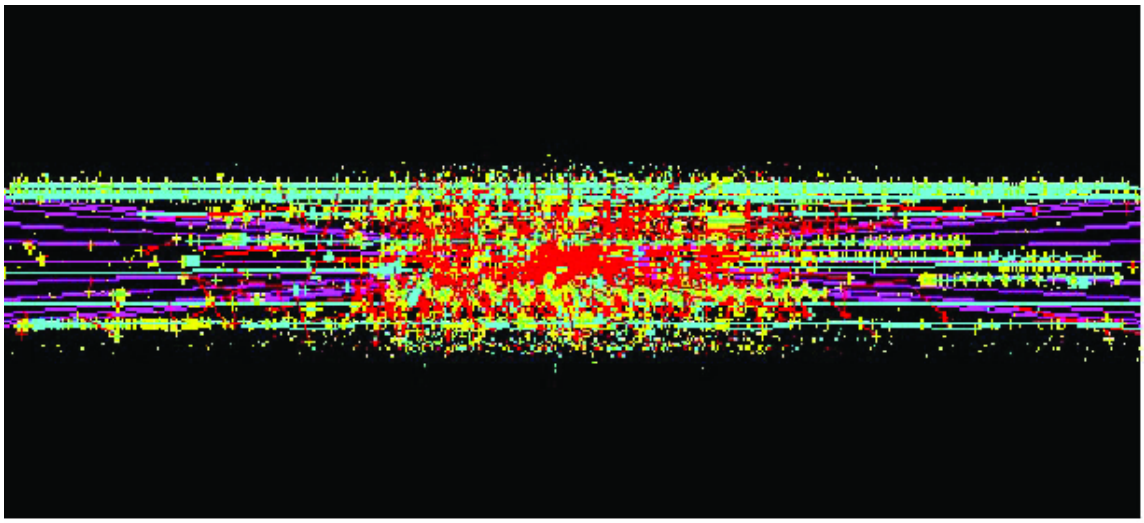

Figure 35. Background hits due to EM particles that pass the $\delta t < 2ns$ cut. The hits are unweighted. In practice there should be $\approx$ 20 times more EM hits. They are concentrated mainly in the EM portion of the calorimeter.

9.4. Muon background

Muons are a result of photons converting (rarely) into a $\mu^+\mu^-$ pair in an electromagnetic shower, and are usually referred to as Bethe Heitler muons. Since the produced muons are unlikely to scatter again, they tend to arrive into the detector rather promptly. Figure 41 shows the muon tracks in the tracker and calorimeter of those that survive he δt <2 ns cut. Figure 42 shows the muon hits that are in time with the traveling gate trigger. Only segments of the muons (that traverse the full length of the calorimeter) survive the traveling gate requirement (as per theorem II). These muon hits are pattern recognizable in the calorimeter offline software and may be further removed from consideration by subtraction.

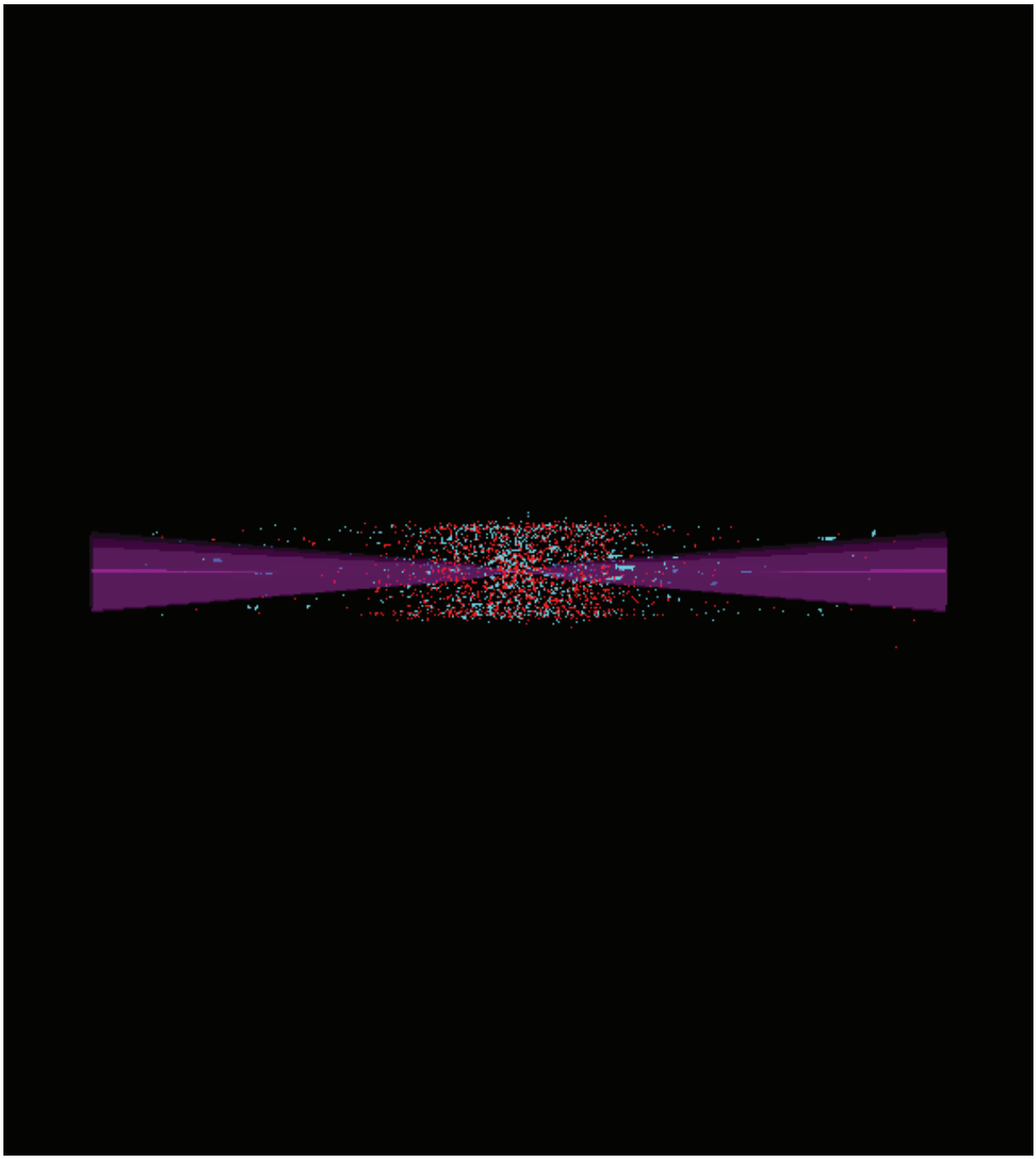

Figure 36. Background hits due to EM particles that pass the $\delta t < 2ns$ cut and are in time with the traveling gate trigger. The hits are unweighted. In practice there should be ≈ 20 times more EM hits. They are concentrated mainly in the EM portion of the calorimeter.

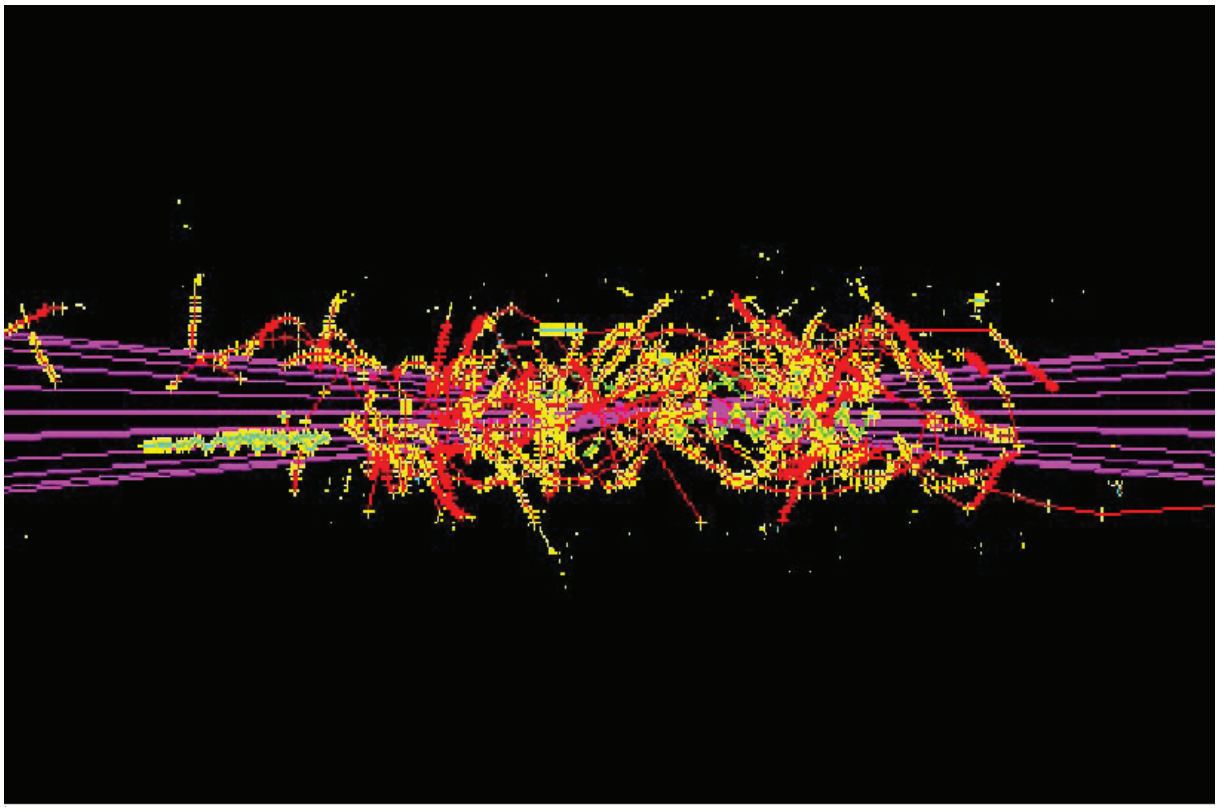

Figure 37. Background hits due to mesons that pass the $\delta t < 2ns$ cut. The hits are unweighted. In practice there should be ≈ 20 times more mesons hits. The mesons appear as background in the tracker as well as the calorimeter.

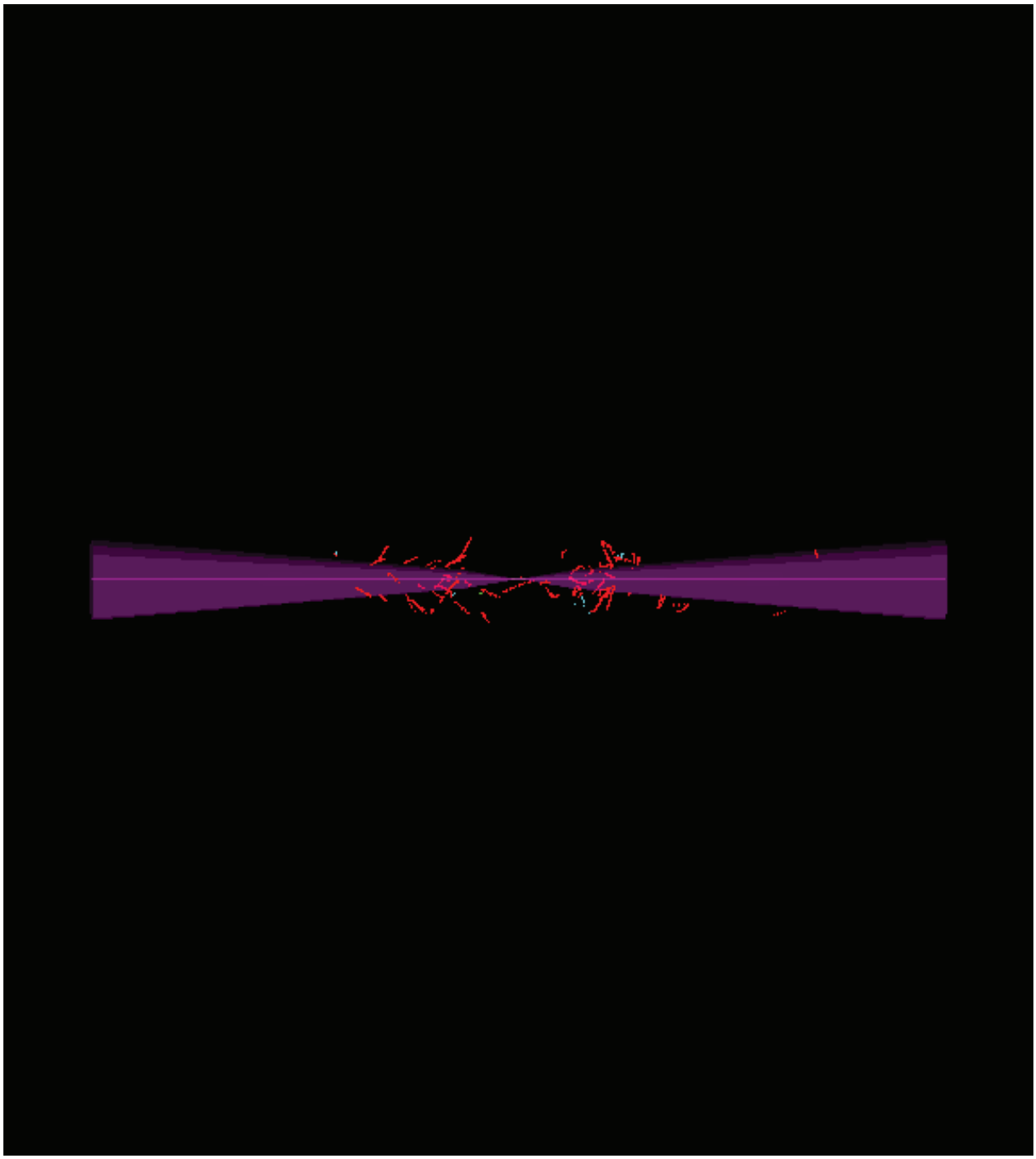

Figure 38. Background hits due to mesons that pass the $\delta t < 2ns$ cut and are in time with the traveling gate trigger. The hits are unweighted. In practice there should be ≈ 20 times more meson hits.

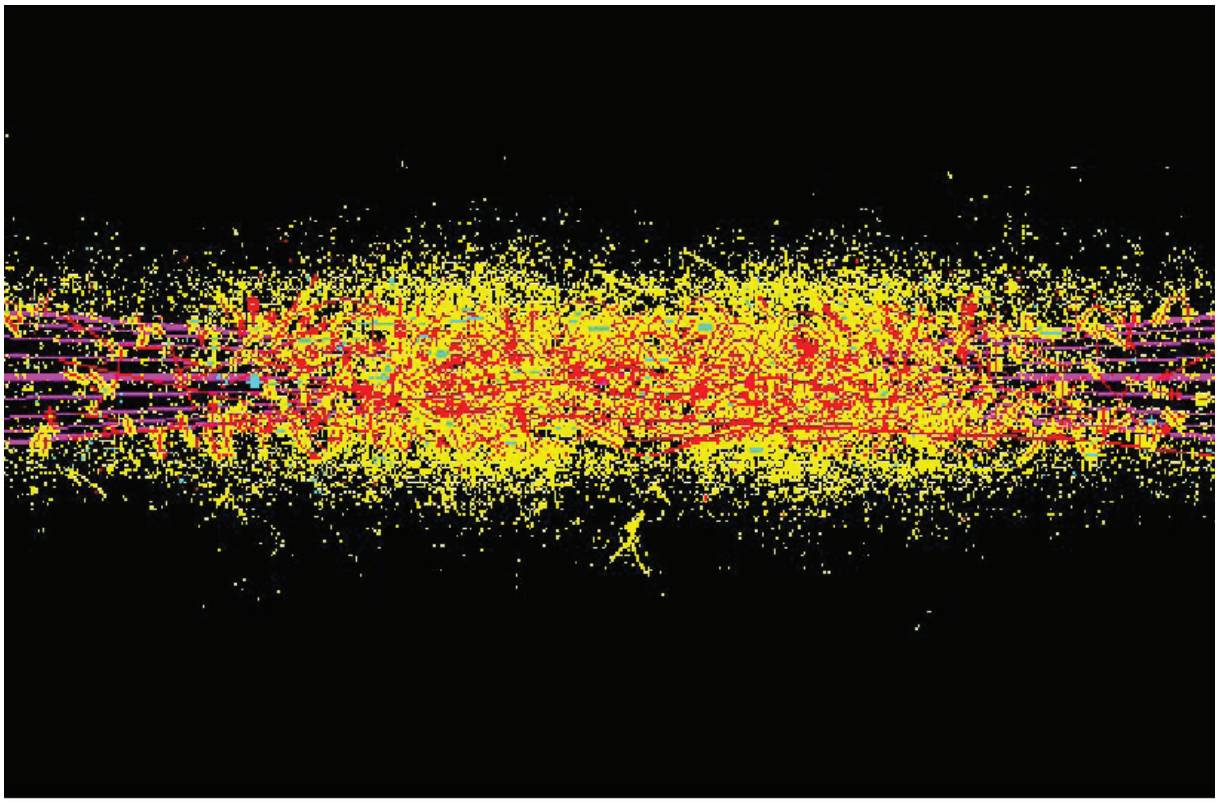

Figure 39. Background hits due to baryons that pass the $\delta t < 2ns$ cut. The hits are unweighted. In practice there should be ≈ 20 times more baryon hits. The baryons (neutrons mostly) appear as background mostly in the calorimeter.

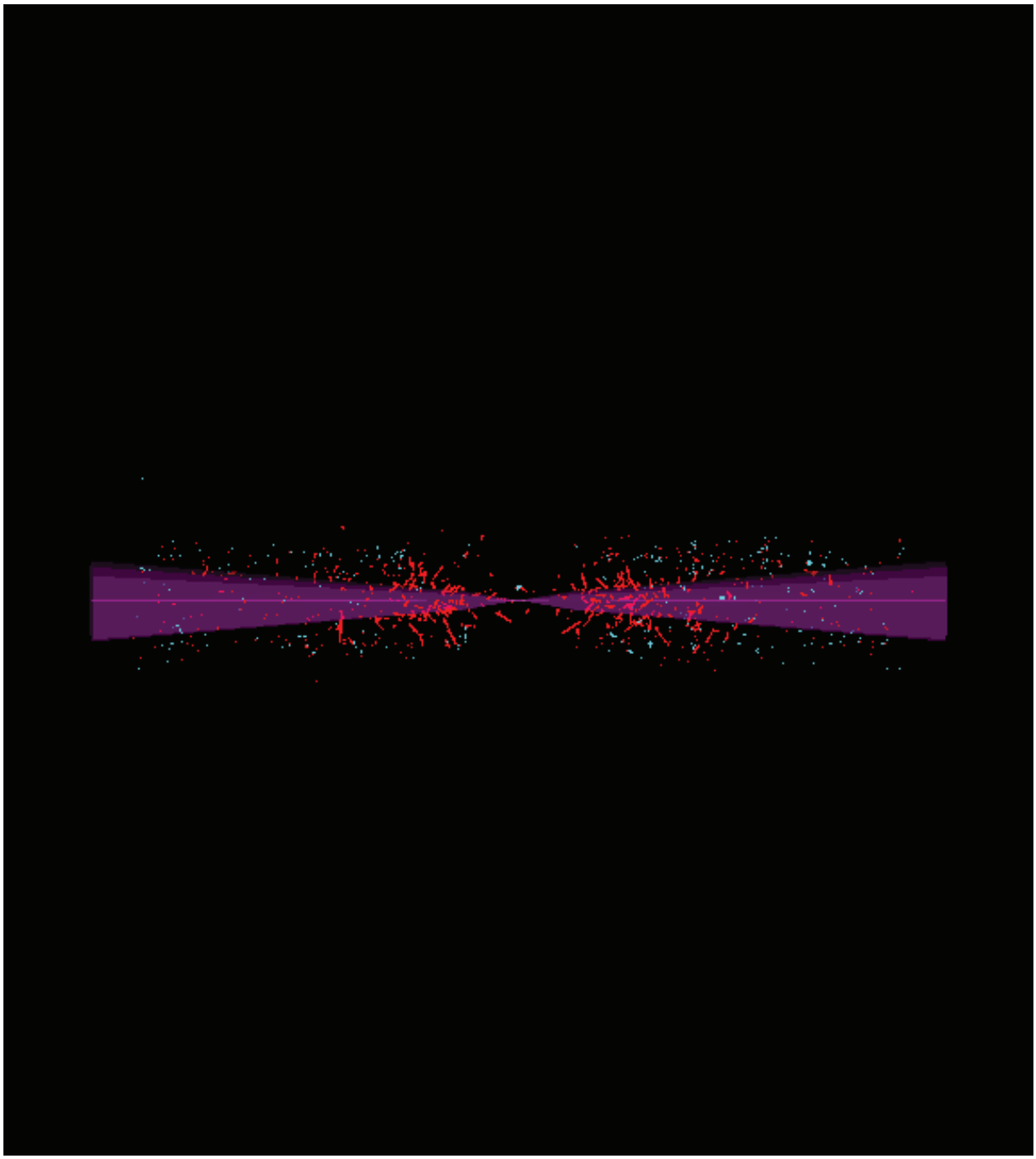

Figure 40. Background hits due to baryons that pass the $\delta t < 2ns$ cut and are in time with the traveling gate trigger. The hits are unweighted. In practice there should be ≈ 20 times more baryon hits.

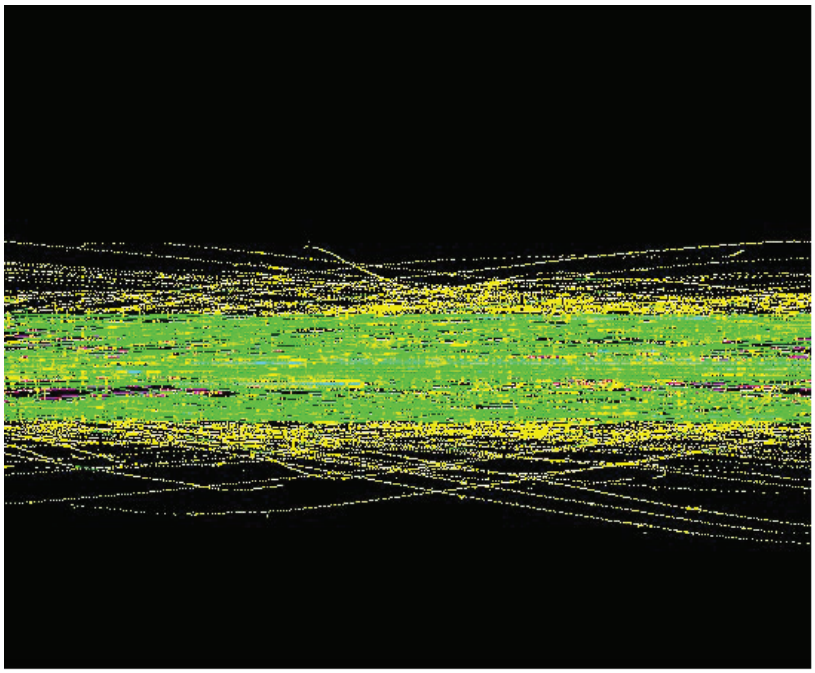

Figure 41. Background hits due to muons that pass the $\delta t < 2ns$ cut. The hits are unweighted. The muons appear as background in the tracker as well as the calorimeter.

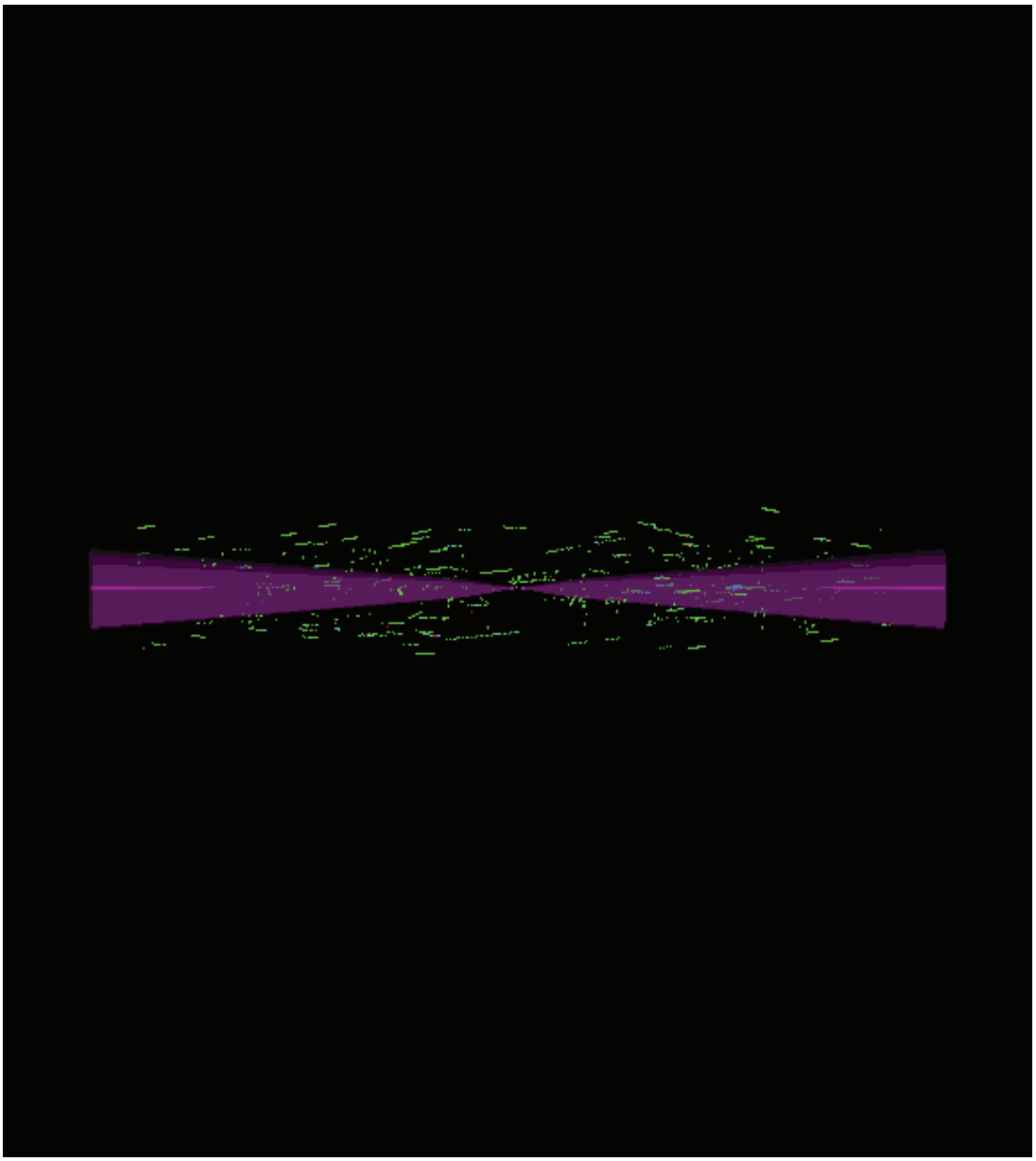

Figure 42. Background hits due to muons that pass the $\delta t < 2ns$ cut and are in time with the traveling gate trigger. The hits are unweighted. There should be an average weight of ≈ 4 for the muons.

Backgrounds before and after time cuts						
Particle Type	**Total before cuts**	**δ t < 2 ns**	**fraction**	**Energy after δ t cut GeV**	**Energy In time GeV**	**Overall Energy Reduction fraction**
EM	1.79E+08	2.17E+06	1.21E-02	962	404.7	2.38E-03
MUONS	8.02E+03	1.83E+03	2.28E-01	1680.9	47.1	2.55E-04
MESONS	1.76E+04	2.66E+03	1.51E-01	270.1	50.7	7.49E-03
BARYONS	4.09E+07	3.93E+05	9.62E-03	8416.8	385.6	2.17E-03

Table 4. Backgrounds as a function of time cuts and the reduction factors associated with each cut.

10. Kinematic Distributions of Backgrounds

We now examine the kinematic distributions of the background hits that survive the $\delta t < 2$ ns cut and those that then survive the traveling gate trigger requirement. Figure 43 shows the pseudo-rapidity of the hits in the calorimeter for both conditions for the four particle types. It can be seen that the traveling gate trigger requirement results in a significant further reduction of the background. The histograms are weighted correctly and show the absolute numbers expected per crossing. Figure 44 shows the momentum distribution of the tracks that cause hits that pass the δt <2 ns cut and the traveling gate trigger requirement. EM and Baryon hits are low momentum where as Meson and Muon hits are due to higher momentum tracks. All histograms are weighted. Figure 45 shows the calorimeter layer of the hits in question. The calorimeter has 340 radial layers with layer 1 being closest to the interaction region. The first 100 layers have 22 radiation lengths and are the EM layers. It can be seen that the EM layers bear the brunt of the background in the calorimeter, in effect acting as further shielding against EM particles and baryons. Figure 46 shows the combined in time background hits as a function of layer number. Most of the hits are concentrated in the first few layers of the EM and are indeed EM particles.

Table 4 shows the backgrounds before and after the time cuts as a function of particle type. For the EM particles, for example, there are 1.79×10^8 particles entering the detector volume. After the $\delta t < 2$ ns cut, only 2.17×10^6 particles survive. The survival fraction at this stage is 1.21×10^{-2}. The energy of these particles is 962 GeV. After requiring them to be in time with the traveling gate, there remains 404.7 GeV of energy still in the calorimeter. This is an overall reduction (in terms of energy) of 2.38×10^{-3}.

This is to be compared with a raw 170 TeV of energy in EM particles before any cuts. The table contains similar information on the remaining particle types.

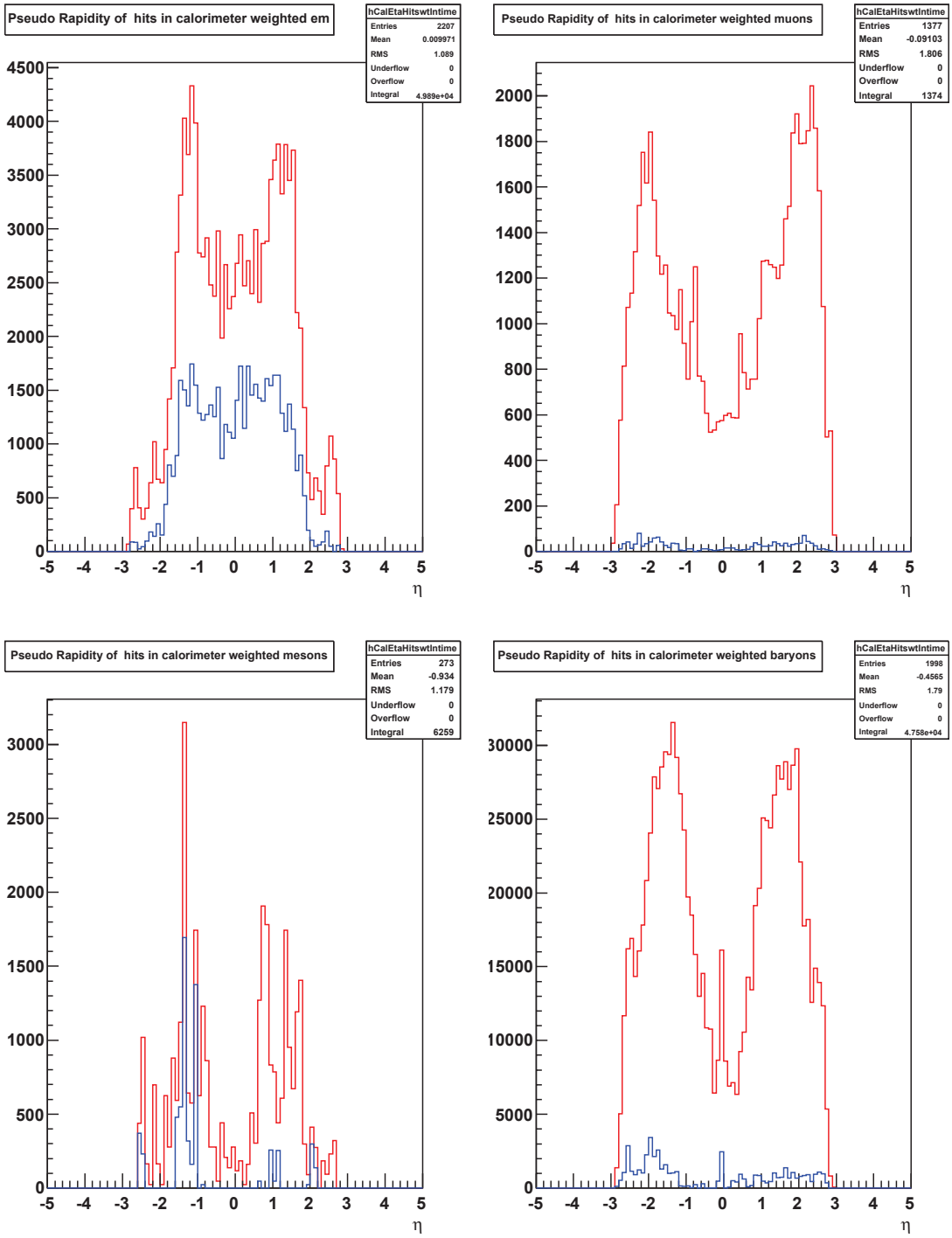

Figure 43. Pseudo-rapidity of backgrounds for EM, Muons, Mesons and Baryons that pass $\delta t < 2ns$ cut(red) and those that are in time (accepted by the traveling gate trigger)(blue). Weighted events used.

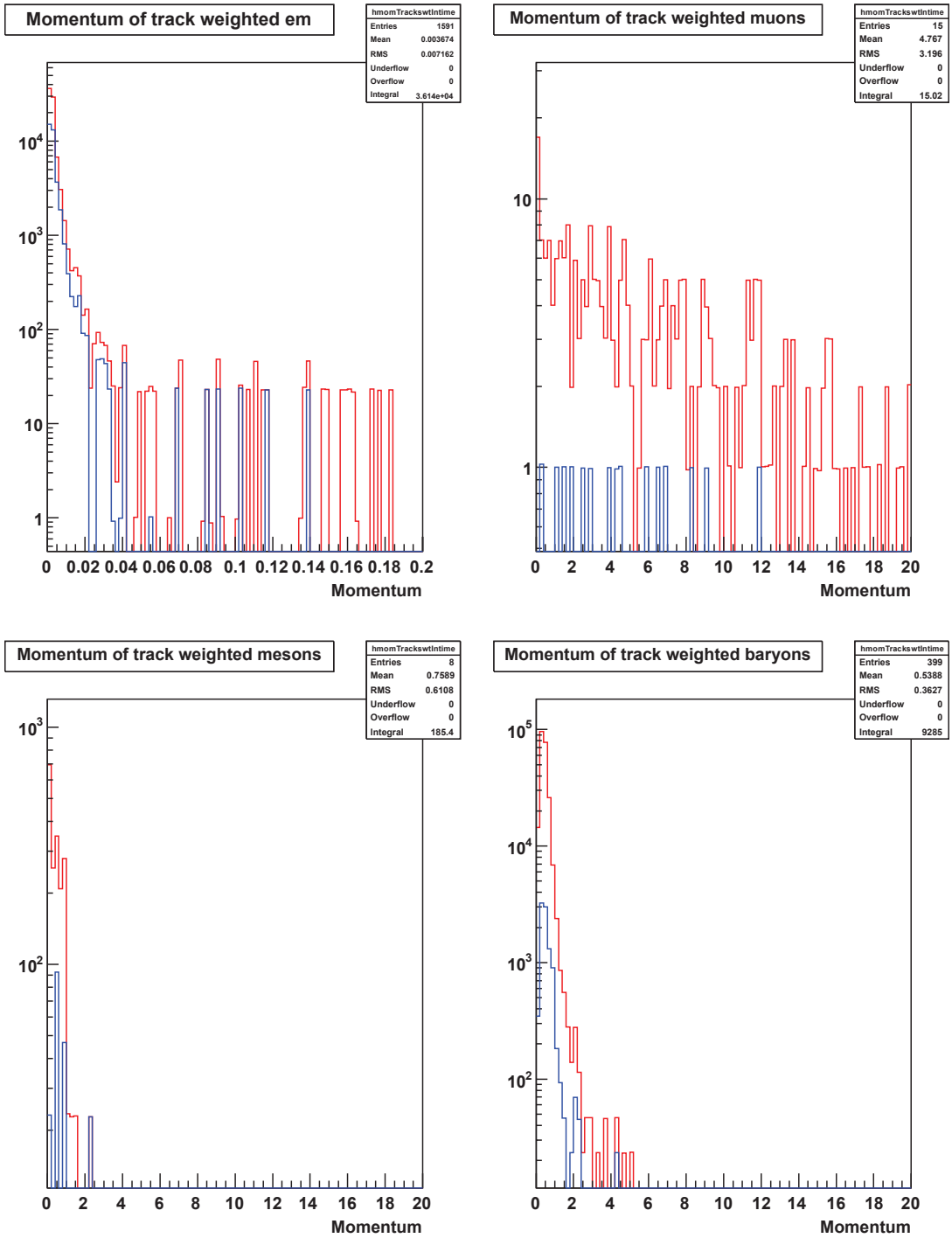

Figure 44. Momentum distribution for EM, Muons, Mesons and Baryons that pass $\delta t < 2ns$ cut (red) and those that are in time (accepted by the traveling gate trigger)(blue). Weighted events used.

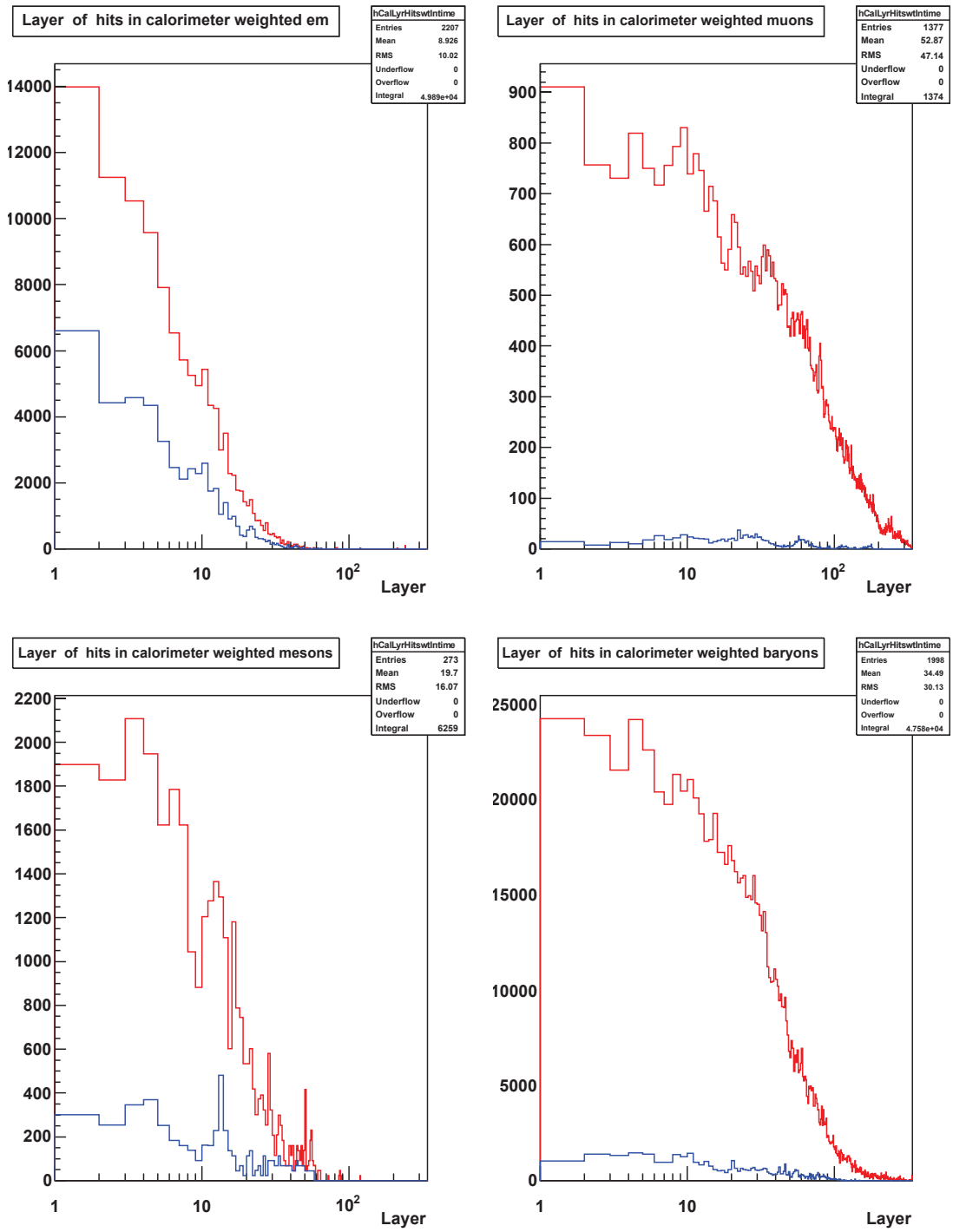

Figure 45. Calorimeter layer number of backgrounds for EM, Muons, Mesons and Baryons that pass $\delta t < 2ns$ cut (red) and those that are in time (accepted by the traveling gate trigger)(blue). There are 340 calorimeter layers. The first 100 constitute the EM section of the calorimeter. Weighted events used.

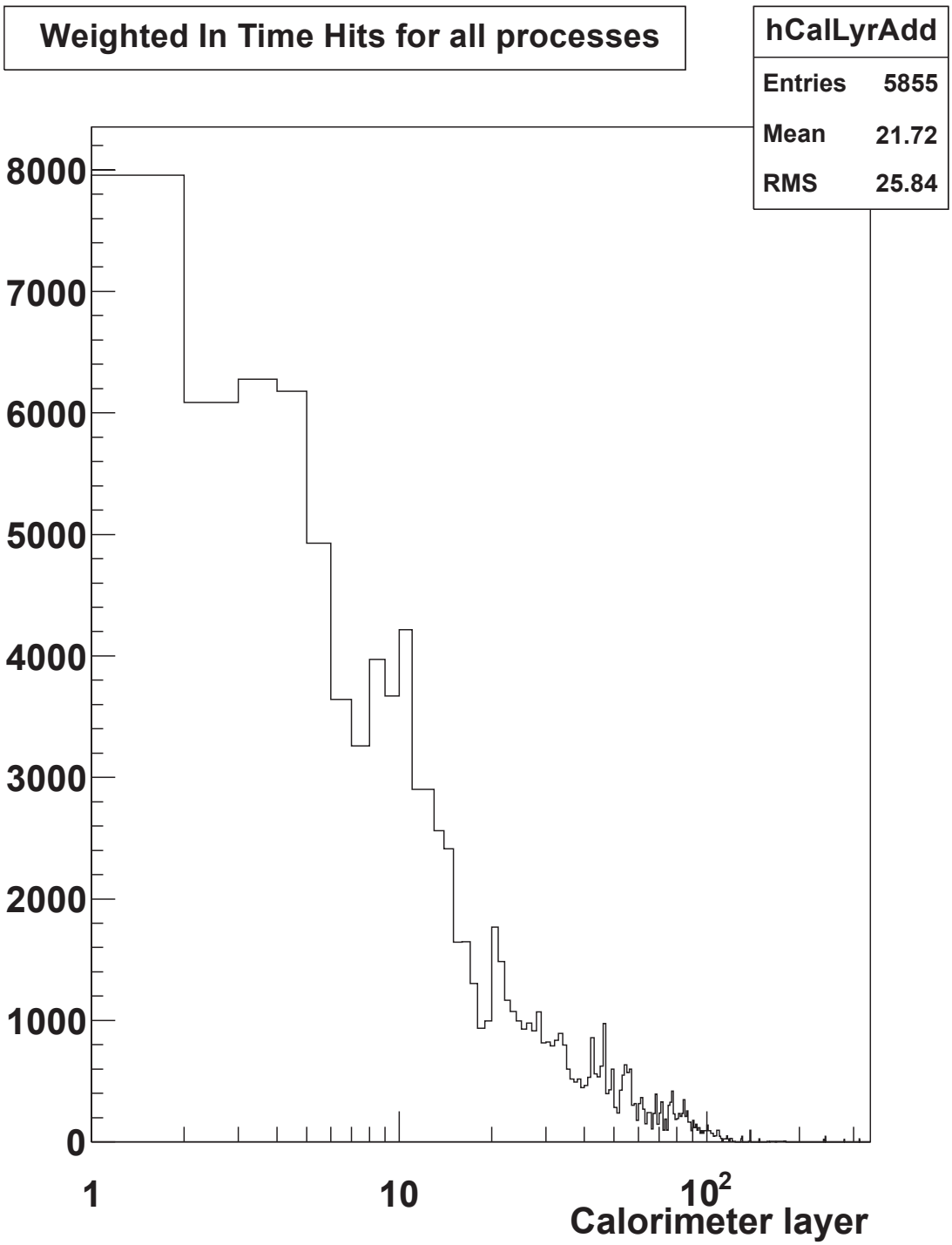

Figure 46. Combined calorimeter layer number of backgrounds that are in time (accepted by the traveling gate trigger). There are 340 calorimeter layers. The first 100 constitute the EM section of the calorimeter. Weighted events used. Note the total hits per layer decrease from 8000 in layer 1 to 1000 by layer 20. This means that most of the background hits are stopped by the first few layers of the EM

11. Signal event

Figure 47 shows a signal event from the process $\mu^+\mu^- \rightarrow$ Higgs by WW fusion. The Higgs mass is taken to be 120 GeV. Notice the excellent granularity of the detector and the resulting ability to pattern recognize the individual tracks and calorimeter deposits of energy as pointing to the interaction region. This ability alone will result in further elimination of background.

In order to further appreciate the signal and background samples we have created a web page, where the individual hits that are in time with the traveling gate trigger are displayed in 3D and rotated. These plots can be found at [14].

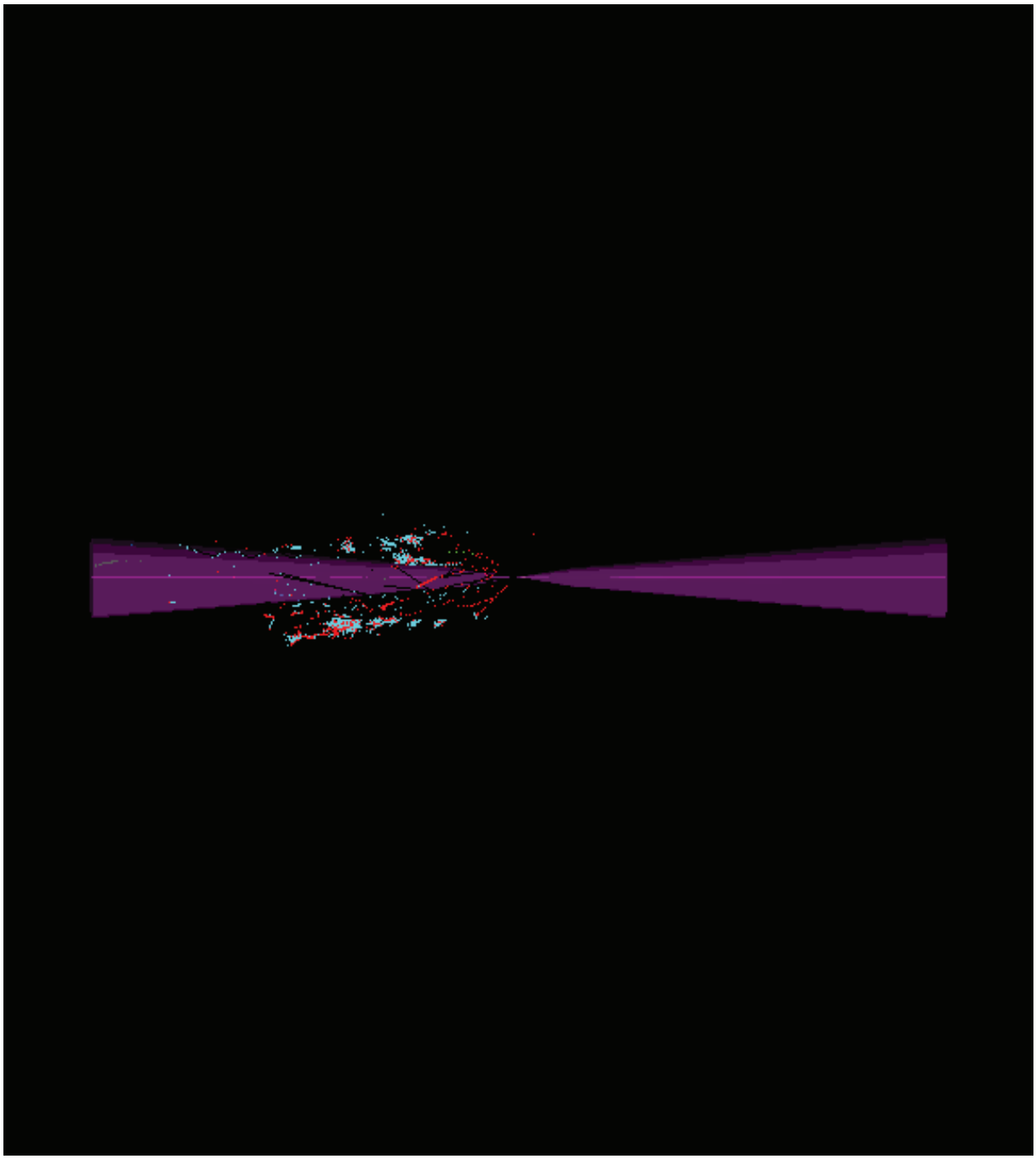

Figure 47. A typical physics event due to the process $\mu^+\mu^- \rightarrow Higgs$ by WW fusion at 1.5 TeV Center of Mass. The muons emit neutrinos which gives the event unbalances longitudinal as well as transverse momentum.

12. Pattern Recognition

The total number of weighted events in time events in layer 1 of the calorimeter is 8000. The total number of pixels in layer 1 is 1.99×10^9. This is an occupancy rate of 4.0×10^{-6}. Total number of hits from the background is 105,000 mostly in EM layers. We expect the pattern recognition to proceed as follows.

Moliere radius background analysis		
Particle Type	**In Moliere Volume MeV**	**In Time MeV**
EM	136.42	57.58
MUONS	103.2	2.19
MESONS	17.05	3.2
BARYONS	852.62	39.07
Total (MeV)		102.05 ± 29

Table 5. Moliere Radius analysis of background in a 100 GeV electron shower.

The pattern recognition for neutral particles from the event proceeds using a Hough algorithm. The particles go in a straight line from the interaction point and are detected in the calorimeter. For EM particles, the Hough width will be the Moliere radius of the electron. The background forms a fuzz where as a signal forms a distinct peak when the Hough algorithm is centered around the primary vertex. Similarly, the neutral non-EM particles from the primary vertex can be detected by varying width Hough algorithms.

The charged particles can be track followed from the vertex and when they enter the calorimeter, their point of entry forms other Hough points which can be used to get the neutral deposits. The charged energy deposits can be pattern recognized by track following the charged tracks in the calorimeter.

The hits from the background fall off by a factor of 1/8 in 20 layers from layer 1. None of the background points to the vertex and the segmentation of calorimeter is a great plus in the regard.

It is worth analyzing the amount of background noise that are deposited in an electron placed at the most difficult point in the calorimeter.

13. Moliere Radius Analysis

As can be seen from Figure 43, the pseudo-rapidity of the EM background peaks around ± 1.1. The hadronic tracks in a signal event in the calorimeter can be track-followed by a pattern recognition program and as such there is little risk of background hits from EM and baryons (the predominant background) to be confused in hadronic signal activity. However, if there is an electron shower in the signal event, it is necessary to estimate the background hits that will be superimposed on the shower. We place an electron shower at the pseudo-rapidity of 1.1, where the maximum of the EM background is to be found. We then draw a cylinder of radius 6 cm around the axis of the electron shower and 100 layers deep (6 cm is slightly larger than the Moliere radius in iron) and estimate the amount of background in this cylinder. Table 5 shows the contribution of the various background types to the Moliere volume. The bottom line is that there is 102 MeV of energy in the Moliere volume due to backgrounds that is in time with the traveling gate. This energy will fluctuate by ±29 MeV. This is at the worst spot for the backgrounds. The 102 MeV can be calibrated out and only its fluctuation need worry us. This is an entirely manageable amount.

14. Jet Finding Algorithms

Since each particle is individually visible, whether neutral or charged, jet cones become obsolete. Particles may be individually associated with jets using proximity criteria. Systematics due to jet cones become a thing of the past.

15. Other Potential Applications to the Travelling Gate Trigger

It is possible to design travelling gate triggers in future neutrino detectors where the event deposition in the far detector can be tied to a micro-bucket of the neutrino beam and a travelling gate of 2 ns or slightly higher can permit the detector to operate at depths far nearer the surface obviating the need for deep mines and cosmic ray vetoes. Each longitudinal segment of the detector will have a travelling gate that is slightly later than the one before it.

16. Conclusions

In conclusion, we have demonstrated a calorimetric system that can function effectively in an environment of the muon collider detector that is highly detector unfriendly in terms of unwanted background due to the interaction of muon decay products in the shielding. This is achieved by a highly pixelated system of calorimetry where each pixel is individually triggerable. We have introduced the concept of the traveling gate trigger which permits the entire calorimeter to be live for only 2 ns but at different times. This results in a significant reduction in the muon collider background. The remaining backgrounds can be pattern recognized away, again utilizing the excellent granularity of the calorimeter.

The excellent granularity of the calorimeter permits various software compensation schemes. We demonstrate a new compensation scheme, based on counting the number of hadronic vertices, which may find application in other hight resolution calorimetry such as liquid argon TPC's.

Compensated calorimetry permit 2 ns timings to produce its resolution. This has implications to other detectors such as CLIC where the issue of 2 ns or 100 ns is of importance to the background from nearby bunches.

The calorimeter does not need a muon system.

We have not insisted on the pixel idea being silicon pixels. Silicon photomultipliers may be another option. Cost and radiation hardness have not been considered in this paper, which merely explores the requirements of a system that can function effectively in the muon collider environment. Inkjet printing [15]of circuits holds promise to be able to produce pixel circuits at much reduced cost. Much R&D is needed to bring these concepts to reality.

17. Acknowledgements

Fermilab is operated Operated by Fermi Research Alliance, LLC under Contract No. DE-AC02-07CH11359 with the United States Department of Energy. The author wishes to thank David Christian and Ronald Lipton for useful discussions on silicon pixel timing capabilities. The author wishes to thank Philippe Canal and Matevz Tadel on help with ROOT 3D graphics.

18. References

[1] In this study we have not optimized the pixel size. We investigate the performance of a calorimeter with 200 micron linear silicon pixels. In practice, the actual pixel size may turn out to be much larger depending on the electronic circuitry, leading to saving in channel count.

[2] Y. I. Alexahin et al.,"Muon Collider interaction region design", Phys.Rev.ST Accel.Beams 14:061001,2011

[3] N. V. Mokhov, S. I. Striganov "Detector background at Muon Colliders" Fermilab-PUB-11-483-APC, 2011.

[4] N. V. Mokhov, "The Mars Code System User's Guide", Fermilab-FN-628 (1995);
N. V. Mokhov, S. I. Striganov, "MARS15 Overview", Fermilab-Conf-07/008-AD (2007);
in Proc. of Hadronic Shower Simulation Workshop, Fermilab, September 2006, AIP Conf. Proc. 896, pp. 50-60 (2007); `http://www-ap.fnal.gov/MARS/`.

[5] The version of Geant3 that has data driven geometry is described in `http://ppd.fnal.gov/experiments/e907/MC/e907mc_doc.htm`

[6] ROOT is a widely used object-oriented program for analysis that uses C_{++}. Documentation can be found at `http://root.cern.ch/drupal/content/users-guide`.

[7] MIPP offline software is documented at `http://ppd.fnal.gov/experiments/e907/OfflineSoftware/`.

[8] H. Bethe, Ann. Phys.5, 325 (1930).
H. H. Andersen and J. F. Ziegler, Hydrogen: Stopping Powers and Ranges in All Elements. Vol 3 of Stopping and Ranges of Ions in Matter (Pergamon press 1977).
[9] See Calorimeter-Energy Measurement in Particle Physics. R Wigmans, Oxford Science Publications, Page 71.
[10] Zeus Uranium calorimeter performance can be found at A. Andersen et al, NIM A290:95,1990.
[11] "Hadron and jet detection with a dual-readout calorimeter", N. Akchurin et. al, NIMA, Volume **537**, Issue 3, (2005) P.537..
[12] "Status of the Icarus Experiment", P. R. Sala for the collaboration, Nucl.Phys.Proc. Suppl.217: (186-188), 2011.
"ArgoNeut and MicroBoone: LAr-TPC's at Fermilab", M. Antonello for the collaboration, AIP Conf. Proc. 1222:257-261, 2010.
[13] "On Sampling fractions and electron shower shapes", A. Peryshkin, R. Raja, paper submitted to NIM.
[14] For a 3D rendition of the backgrounds see `http://ppd.fnal.gov/experiments/e907/raja/MuonColliderW&C/Muon3D.html`
[15] "Inkjet printing used to create graphene-based circuits", `http://www.theverge.com/2011/11/26/2587718/inkjet-print-graphene-circuits-research`.